Integrative Chemical Genetics Platform Identifies Condensate Modulators Linked to Neurological Disorders

Dylan Poch,[1] Chandrayee Mukherjee,[1] Sunanda Mallik,[1] Vanessa Todorow,[1] E.F. Elsiena Kuiper,[1,2] Nalini Dhingra,[3] Yulia V Surovtseva,[3] Christian Schlieker.[1,4,*]

[1]Department of Molecular Biophysics and Biochemistry, Yale University, New Haven, CT 06511, USA.
[2]Max Planck Institute of Biophysics, Mechanisms of Cellular Quality Control, Frankfurt a. M., Germany
[3]Yale Center for Molecular Discovery, Yale University, West Haven, CT 06516, USA.
[4]Department of Cell Biology, Yale School of Medicine, New Haven, CT 06520, USA.

*Correspondence: christian.schlieker@yale.edu

HIGHLIGHTS

- MLF2 emerges as a disease-agnostic condensate biomarker co-localizing with TDP-43 and G3BP1
- FDA-approved drugs target condensates linked to perturbed proteostasis.
- RNF26 and ZNF335 are identified as modulators of nuclear phase transitions.
- Microcephaly patient disease alleles fail to counteract aberrant condensates.

ABSTRACT

Aberrant biomolecular condensates are implicated in multiple incurable neurological disorders, including Amyotrophic Lateral Sclerosis (ALS), Frontotemporal Dementia (FTD), and DYT1 dystonia. However, the role of condensates in driving disease etiology remains poorly understood. Here, we identify myeloid leukemia factor 2 (MLF2) as a disease-agnostic biomarker for phase transitions, including stress granules and nuclear condensates associated with dystonia. Exploiting fluorophore-derivatized MLF2 constructs, we developed a high-content platform and computational pipeline to screen modulators of NE condensates across chemical and genetic space. We identified RNF26 and ZNF335 as protective factors that prevent the buildup of nuclear condensates sequestering K48-linked polyubiquitinated proteins. Chemical screening identified four FDA-approved drugs that potently modulate condensates by resolving polyubiquitinated cargo and MLF2 accumulation. Our exploratory integrated chemical-genetics approach suggests that modulation of zinc, and potentially autophagy and oxidative stress, is critical for condensate modulation and nuclear proteostasis, offering potential therapeutic strategies for neurological disorders. Application of our platform to a genome-wide CRISPR KO screen identified strong enrichment of candidate genes linked to primary microcephaly and related neurodevelopmental disorders. Two hypomorphic microcephaly-associated alleles of ZNF335 failed to rescue nuclear condensate accumulation in ZNF335 KO cells, suggesting that aberrant condensates and impaired nuclear proteostasis may contribute to the pathogenesis of microcephaly.

KEYWORDS

High-content screening, dystonia, ALS/FTD, biomolecular condensates, MLF2, RNF26, ZNF335, pyrithione zinc, stress granules, microcephaly.

INTRODUCTION

Aberrant biomolecular condensates are drivers for many neurological disorders, including Amyotrophic Lateral Sclerosis (ALS), Frontotemporal Dementia (FTD), and DYT1 dystonia.[1–5] Biomolecular condensates, often made from a milieu of hundreds of different proteins, consist of a thermodynamically favorable dense phase and dilute phase.[6,7,8,9] When properly regulated, biomolecular condensates allow efficient, fine-tuned microenvironments, ensuring maintenance of cellular homeostasis while buffering against external perturbations.[10–12] However, in pathological states sometimes referred to as condensatopathies, these condensates exhibit reduced dynamicity and undergo aberrant phase-transitions, leading to protein aggregation or amyloid formation that is not easily reversible.[13–15] It is estimated that up to one-third of common diseases can be potentially linked to condensate-forming proteins.[16] Which mechanisms and cellular activities establish and maintain condensates in a functional state are currently critical questions. A deeper understanding of these processes is essential for devising therapeutic strategies that tune condensate properties to counteract transitions to non-functional or toxic states.

One “favorable” phase-state is observed in the central channel of the nuclear pore complex (NPC). The NPC serves as the intermediary gate at which nuclear transcription is separated from cytoplasmic translation in eukaryotic organisms. Crudely, the NPC features ring-like structures that surround a central transport channel enriched in phenylalanine-glycine nucleoporins (FG-nups) with a high number of intrinsically disordered regions (IDRs). The IDR FG-repeat moieties of the FG-nups, along with importins and exportins, constitute a “phase” state (described as a hydrogel-like, polymer brush or as a selective phase model, among others), contributing to the selective barrier of the NPC.[17–23] Recently, it has been proposed that this phase state results in an optimal environment that counteracts protein aggregation and promotes folding.[24] However, disruptions to NPC assembly or nucleocytoplasmic transport have been strongly implicated in neurological diseases, including Alzheimer’s disease, ALS/FTD, Huntington’s disease, and dystonia.[1,25–29] As neurons are primarily limited to interphase “inside-out” NPC biogenesis,[30,31] dysregulation of this mode of NPC biogenesis can pathologically sensitize neurons toward disease.[1,32]

DYT1 dystonia is a debilitating and currently incurable movement disorder characterized by involuntary muscle contractions and painful sustained postures,[33,34] which has been linked to NPC perturbation.[1,32] There are no curative or preventative treatments for dystonia, current interventions remain palliative.[33,34] DYT1 dystonia is caused by an autosomal dominant GAG deletion (ΔE) within the TOR1A gene that disrupts ATPase activation in this AAA+ ATPase.[35–39] The ΔE mutation or deletion of TorsinA results in aberrant deposition of both FG-nups and enrichment of K48-linked ubiquitinated (K48-Ub) proteins within nuclear envelope (NE) condensates,[1,40] resulting from aberrant NPC assembly,[41] leading to mislocalization and delay of NPC biogenesis in mouse models of dystonia.[32] This NE condensate phenotype or other NE and nuclear transport abnormalities are recapitulated in various disease models, including *Caenorhabditis elegans*,[42] *Drosophila melanogaster*,[43] and human induced pluripotent stem cell (iPSC) lines.[44] Previously, our lab developed a cell-based DYT1 model system by deleting TOR1A and its functionally redundant paralogs (TOR1B, TOR2A, TOR3A) in HeLa cells (4TorKO cells),[41] resulting in an NE condensate phenotype analogous to those observed in the DYT1 dystonia mutation.[1,40,45]

We identified two major proteotoxic outcomes of these aberrant NE condensates in 4TorKO cells and primary mouse neurons: (i) the accumulation of ubiquitinated and potentially proteotoxic proteins at the NE and (ii) the sequestration of a chaperone network (HSPA1A, HSC70, DNAJB6, and DNAJB2).[1,40,46] We discovered that these ubiquitylated proteins can evade proteasomal degradation by accumulating in NE condensates, leading to a significantly increased half-life, potentially contributing to protein aggregation.[1] Furthermore, the near-complete sequestration of specific chaperones into NE condensates hinders their ability to maintain cellular protein homeostasis (proteostasis). Therefore, modulating NE condensates by either direct dissolution or modulation of its proteotoxic properties could represent a novel therapeutic approach, an undertaking that would be greatly facilitated by suitable biomarkers for aberrant condensates. Myeloid leukemia factor 2 (MLF2) might be a suitable biomarker candidate for several reasons: (1) MLF2 is a major constituent of NE condensates in 4TorKO cells.[40], and it is (2) highly enriched in Methionine and Arginine,[1] residues which have been suggested to engage in interactions with aromatic side chains in FG-nups.[47] MLF2 readily immerses

63 into FG-nup phases *in vitro* and is required for the interacting protein DNAJB6 to be re-
64 cruited to NE condensates in cells.[1] We exploited these properties to visualize proteo-
65 toxic condensates using fluorescence imaging and designed doxycycline (Dox) induci-
66 ble fluorophore-derivatized variants of MLF2 as a condensate biomarker.[1,40]
67 In this study, we establish MLF2 as a disease-agnostic marker of aberrant con-
68 densates, enriched in proteotoxic nuclear condensates and stress granules, as indi-
69 cated by strong co-localization with TDP-43 and G3BP1. High-content screening using
70 an MLF2-GFP readout identified both pharmacological and previously uncharacterized
71 genetic modulators of aberrant phase transitions. Importantly, we identified several
72 FDA-approved small molecules (pyrithione zinc, celastrol, plumbagin, and disulfiram)
73 along with a zinc-dependent mechanism that decreases nuclear condensate formation
74 in torsin-deficient cells associated with DYT1 dystonia. A genome-wide CRISPR knock-
75 out (KO) screen identified RNF26 and ZNF335 as key regulators protecting against ab-
76 errant condensate formation. Strikingly, 15 out of the top 50 gene hits are strongly asso-
77 ciated with neurodevelopmental disorders, including seven directly linked to primary mi-
78 crocephaly or related developmental disorders. Indeed, hypomorphic disease alleles of
79 ZNF335 implicated in microcephaly progression failed to rescue condensate accumula-
80 tion in ZNF335 KO cells, suggesting a hitherto unknown connection between nuclear
81 condensates, perturbed nuclear proteostasis, and neurodevelopmental disorders.
82
83 **RESULTS**
84 **MLF2 is a Biomarker for Aberrant Condensates Associated with ALS/FTD and**
85 **DYT1 Dystonia.**
86 Having previously established the connection between impaired protein quality control
87 (PQC) and perinuclear condensates in cell-based dystonia models (Figure 1A),[1] we
88 aimed to more broadly identify modulators of nuclear condensates and protein homeo-
89 stasis. Since at least a subset of condensates share aromatic side chains as part of
90 their "molecular grammar",[48] we reasoned that MLF2 might localize to additional aber-
91 rant condensates. Dysregulation of stress granules (SGs) has been pathologically asso-
92 ciated with several neurological disorders, including ALS and FTD.[13] It is well estab-
93 lished that exposing cells to oxidative stress with sodium arsenite ($NaAsO_2$) causes SG

formation.[49–52] To assess the potential co-localization of MLF2 with stress granules, we expressed two common stress granule biomarkers, G3BP1 and TDP-43, after exposing WT HeLa cells to 0.5 mM $NaAsO_2$ for 30 min. Strikingly, MLF2 exhibited strong co-localization with both G3BP1-GFP and TDP-43-tdTomato, regardless of $NaAsO_2$ exposure

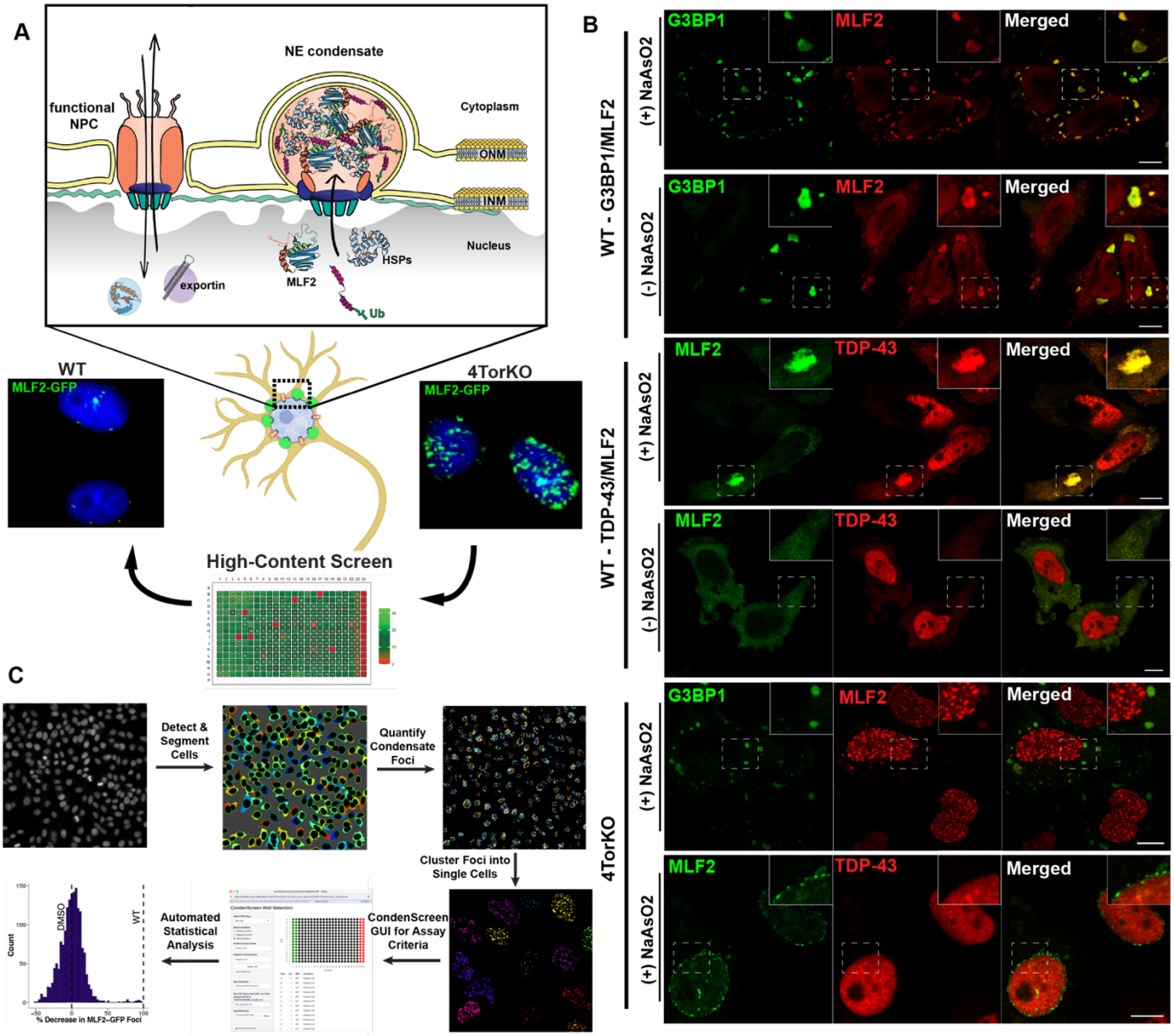

Fig. 1 | **MLF2 is a biomarker for aberrant phase transitions across neurological disorders.** (A) Nuclear envelope condensates develop in DYT1 dystonia models due to torsinA deficiency. MLF2, K48-Ubiquitin enriched proteins, and a network of heat shock proteins are tightly sequestered into the condensates; these can be exploited for high-content imaging platforms. (B) MLF2 co-localizes with both G3BP1 (top panel) and TDP-43 (middle panel) before and after stress granule formation in response to oxidative stress ($NaAsO_2$). MLF2 remains primarily within nuclear envelope condensates in Torsin-deficient cells after oxidative stress (bottom panel, upper (G3BP1) and mid (TDP-43) Z-planes shown for representation). Scale bars, 5 µm. (C) Schematic of computational screening workflow.

98 (Figure 1B). However, while G3BP1 and TDP-43 did not visibly co-localize with NE con-
99 densates in 4TorKO HeLa cells after $NaAsO_2$ treatment, we observed partial trafficking
100 of MLF2 into SGs, though the majority remained confined to pre-formed NE conden-
101 sates. These findings suggest that MLF2 serves as a robust biomarker for multiple
102 types of aberrant condensates in a disease-agnostic manner.
103

104 **Establishing MLF2-GFP as a Robust Readout of Aberrant Condensates for High-**
105 **Content Screening**

106 Leveraging the robust condensate biomarker properties of MLF2-GFP, we devel-
107 oped a miniaturized, high-content microscopy assay using Dox-inducible MLF2-GFP
108 cells in a 384-well format. This facilitated the design of phenotypic, high-content arrayed
109 screens to identify chemical and genetic perturbations that modulate nuclear conden-
110 sates. Specifically, each well contained either a small molecule applied to 4TorKO cells
111 or synthetic single guide RNAs (sgRNAs) targeting a single human gene, delivered to
112 Cas9-integrated WT cells, to either suppress or promote nuclear condensates, respec-
113 tively. After obtaining 10,368 high-resolution images/plate, we employed our customized
114 computational suite, *CondenScreen*—a *CellProfiler* and *R* script condensate screening
115 analysis pipeline—for rapid quantification and statistical analysis of aberrant conden-
116 sates (Figure 1C).

117 While many robust computational resources are available for monitoring conden-
118 sates (see *PhaseMetrics* and *Punctatools*)[53,54], *CondenScreen* is specifically designed
119 for large-scale, high-content screening analysis using a customizable *CellProfiler 4* [55,56]
120 pipeline to determine the number of condensate foci per identified cellular compartment
121 and quantify the robustness of the screen. Each condensate marker is then clustered
122 into its corresponding single cell. To analyze images in parallel, we developed an op-
123 tional Bash script that executes multiple headless *CellProfiler* instances on a Simple
124 Linux Utility for Resource Management (SLURM) cluster. This enables efficient, autono-
125 mous analysis of over 1 million high-content TIFF images—amounting to multiple tera-
126 bytes of data—within hours.

127 Extracted data was analyzed using our custom *R*-script that iteratively groups
128 each cell and returns the aggregated statistics of each perturbation. Results include the

129 average number of foci per cell, size of each foci, percent viability (function of cell count
130 and nuclear area/shape), normalized Z-score (signal "ON" screens) or BZ-score (signal
131 "OFF" screens), and a suite of automatically generated figures. Additionally, it returns
132 plate-wise statistics, including the assay quality score (Z'-score),[57] signal-to-background
133 noise (SB), and the standard deviation (SD) and coefficient of variation (CV) of the con-
134 trols. *CondenScreen* provides a simple graphical user interface (GUI), allowing the user
135 to select plate size, layout, and choose whether their screen was signal "ON" vs a signal
136 "OFF", altering downstream statistics (Figure 1C). To avoid false positives, we quanti-
137 fied the potential influence of differential transcriptional/translational levels by empirically
138 deriving a condensate normalization score (CNS) equation (see methods). Integrating
139 the MLF2-GFP inducible system with our *CondenScreen* analysis pipeline enables rapid
140 phenotypic identification of hits that modulate aberrant condensates.
141

142 **High-Content Screen Identifies FDA-approved Drugs that Modulate NE Conden-**
143 **sates**

144 We screened 1760 drugs from the Pharmakon library in MLF2-GFP inducible 4TorKO
145 HeLa cells, comprising 1360 US and 400 international drugs used at a 10 μM working
146 concentration. One day after seeding 4TorKO HeLa cells in 384-well plates, we induced
147 MLF2-GFP expression (Dox, 0.5 μg/ml) for 6 h before adding compounds. This enabled
148 expression of the MLF2-GFP reporter before adding compounds to minimize false posi-
149 tives due to differential reporter expression.
150 Compounds were added 2 h before fixation, followed by staining, imaging, and
151 analyzing the resulting high-content images with *CondenScreen*. To measure the quality
152 of the screen, we calculated the Z' value to measure the separation between the posi-
153 tive (DMSO-treated WT HeLa) and negative (DMSO-treated 4TorKO HeLa) controls.
154 Our average Z' value was 0.73, well above the literature standard of Z' > 0.5, indicating
155 a robust assay.[57] Additionally, the ratio between the negative and positive controls (SB)
156 was > 930, while the SD and CV of DMSO-treated cells were 2.1% and 9.2%, respec-
157 tively, further confirming assay robustness.

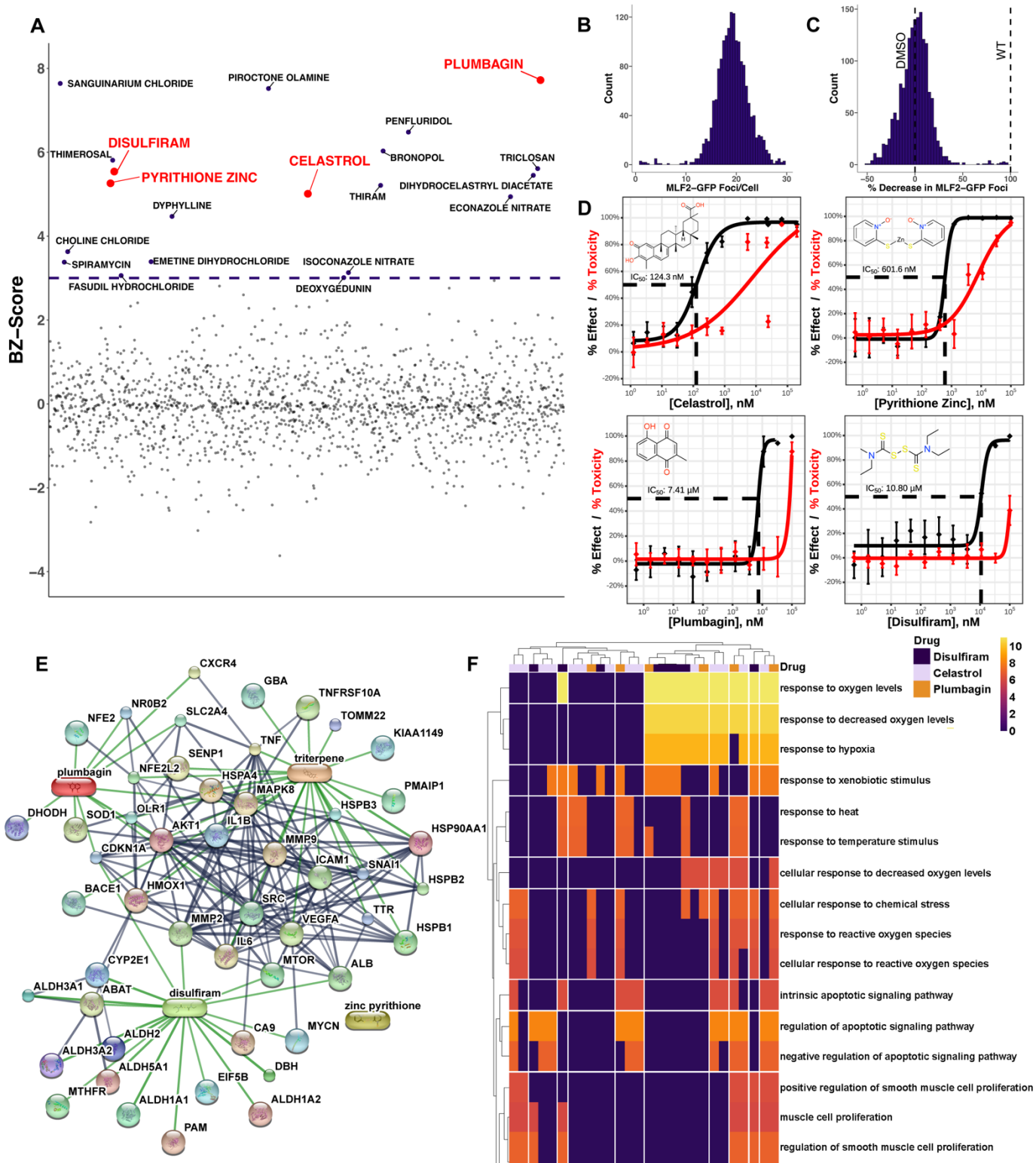
A
BZ–Score
PLUMBAGIN
SANGUINARIUM CHLORIDE
PIROCTONE OLAMINE
PENFLURIDOL
DISULFIRAM
THIMEROSAL
PYRITHIONE ZINC
CELASTROL
BRONOPOL
TRICLOSAN
DIHYDROCELASTRYL DIACETATE
THIRAM
DYPHYLLINE
ECONAZOLE NITRATE
CHOLINE CHLORIDE
SPIRAMYCIN
EMETINE DIHYDROCHLORIDE
ISOCONAZOLE NITRATE
FASUDIL HYDROCHLORIDE
DEOXYGEDUNIN
B
Count
MLF2–GFP Foci/Cell
C
DMSO
WT
Count
% Decrease in MLF2–GFP Foci
D
% Effect / % Toxicity
IC50: 124.3 nM
[Celastrol], nM
IC50: 601.6 nM
[Pyrithione Zinc], nM
IC50: 7.41 µM
[Plumbagin], nM
IC50: 10.80 µM
[Disulfiram], nM
E
CXCR4
GBA
TNFRSF10A
NR0B2
SLC2A4
NFE2
TOMM22
KIAA1149
TNF
SENP1
triterpene
plumbagin
NFE2L2
HSPA4
MAPK8
PMAIP1
HSPB3
DHODH
SOD1
OLR1
AKT1
IL1B
HSP90AA1
CDKN1A
MMP9
ICAM1
SNAI1
HSPB2
BACE1
HMOX1
SRC
TTR
MMP2
VEGFA
HSPB1
IL6
CYP2E1
MTOR
ALB
ALDH3A1
ABAT
disulfiram
zinc pyrithione
CA9
MYCN
ALDH2
ALDH3A2
ALDH5A1
DBH
EIF5B
MTHFR
ALDH1A1
ALDH1A2
PAM
F
Drug
Disulfiram
Celastrol
Plumbagin
response to oxygen levels
response to decreased oxygen levels
response to hypoxia
response to xenobiotic stimulus
response to heat
response to temperature stimulus
cellular response to decreased oxygen levels
cellular response to chemical stress
response to reactive oxygen species
cellular response to reactive oxygen species
intrinsic apoptotic signaling pathway
regulation of apoptotic signaling pathway
negative regulation of apoptotic signaling pathway
positive regulation of smooth muscle cell proliferation
muscle cell proliferation
regulation of smooth muscle cell proliferation
smooth muscle cell proliferation
leukocyte migration
extrinsic apoptotic signaling pathway
regulation of extrinsic apoptotic signaling pathway
MMP9
IL6
DBH
ICAM1
IL1B
CDKN1A
HSP90AA1
HSPB2
MAPK8
ALDH3A1
TNFRSF10A
SOD1
HSPB1
SNAI1
CXCR4
MTHFR
CA9
ABAT
MTOR
VEGFA
SLC2A4
NFE2L2
PMAIP1
AKT1
HMOX1
MMP2
TNF
SRC

Fig. 2 | **Drug screen identifies compounds decreasing MLF2-GFP accumulation within NE condensates** (A) Scatter plot of compounds modulating MLF2-GFP accumulation of 4TorKO HeLa cells. Drugs (circles) passing significance threshold (dotted-line, BZ-score > 3) are labeled purple, while red-labeled dots denote drugs selected for downstream validation. (B) Histogram of the distribution in the average MLF2-GFP foci/cell. (C) Histogram of the percent decrease of MLF2-GFP foci per cell normalized to the mean of the screening population. (D) Calculated IC_{50} values of four drugs with prominent dose-response relationships. Determined IC_{50} from 12-point dose response (four orders of magnitude, n = 4). Black line represents % effect (decrease in MLF2-GFP foci), red line represents % toxicity relative to DMSO (four-parameter-log-logistic model). (E) Interaction network of proteins predicted to interact with plumbagin, disulfiram, PZ, and celastrol (triterpene) using STITCH analysis. Limited to top 50 high confidence (0.7) predicted interactions. Gray and green lines represent protein-protein and protein-chemical interactions, respectively. Thicker lines represent stronger associations. (F) Heatmap of the 20 top biological processes (rows) and enriched predicted interactors (columns) from STITCH analysis. GO analysis compared enriched predicted proteins against the org.Hs.eg.db gene set. Color scale legend indicates -log(10) Benjamini-Hochberg adjusted p-value, with lighter regions being more significant. Corresponding drugs at top in light purple (celastrol), black (disulfiram), or orange (plumbagin). Euclidian distance hierarchical clustering for GO-enriched biological pathways and genes products are shown with the left and top dendrogram, respectively.

To control for plate-specific column, row, and edge, we assigned each compound a BZ-score based on its normalized effect on reducing the number of MLF2-GFP foci (Figure 2A, see methods). The distribution of the data indicated a slight negative skew in the average number of MLF2-GFP foci per condition (Figures 2B, 2C). Using a cutoff BZ-score of three, we identified 20 putative hit compounds that significantly depleted MLF2-GFP NE condensate foci. The top ranked compounds included plumbagin, sanguinarium chloride, thiram, piroctone olamine, penfluridol, bronopol, thimerosal, triclosan, disulfiram, celastrol, dihydrocelastryl diacetate, and pyrithione zinc (PZ). A full list of the screened drugs can be found in the supplementary materials (Table S1).

Top-scoring compounds were repurchased and resolubilized to construct a 12-point dose-response (n = 4 replicates), covering over 5 orders of magnitude to determine the calculated IC_{50}. (Figure 2D, Figure S1A). The normalized percent effect and percent toxicity (calculated as a function of viability and changes to nuclear area and morphology relative to DMSO control) were quantified for each concentration to determine potential therapeutic windows. Out of the tested compounds, the four structurally diverse drugs with the greatest dose-dependent relationship were celastrol (IC_{50} = 124.3 nM), PZ (IC_{50} = 601.6 nM), plumbagin (IC_{50} = 7.4 μM), and disulfiram (IC_{50} = 10.8 μM) (Figure 2D).

We used the search tool for interactions of chemical (STITCH) database to probe high-confidence potential direct or indirect functional partners of the four most promising compounds (Figure 2E)[58] Based on the top predicted functional partners, we used Gene Ontology (GO) to identify enriched biological processes with the highest statistical significance (q-value < 0.05) (Figure 2F).[59,60] Pathways were further manually classified into the following seven categories: Response to Oxygen/Oxidative Stress, Response to

182 Heat, Response to Chemical Stimulus, Apoptotic Signaling, Cellular Migration, Cellular
183 Proliferation, and Other (Figure S1B). While exploratory, these data suggest modulation
184 of stress may critically alter the properties of NE condensates, consistent with our ear-
185 lier observation of NE condensate enlargement following heat shock.[61]
186
187 **Pyrithione Zinc Depletes NE Condensate Biomarkers Independent of Differential**
188 **Protein Expression**
189 To determine the optimal concentration, we tested each of the four candidate com-
190 pounds—celastrol, PZ, plumbagin, and disulfiram—at four tighter concentrations, includ-
191 ing the IC_{50} itself, at 2x above/below the IC_{50}, and 8x above the IC_{50} concentrations, us-
192 ing a 3 h compound treatment. The resulting boxplot reflects each compound's effect at
193 the single-cell level (Figure 3A). Consistent with the significant cell-cycle dependency of
194 NE condensate formation previously demonstrated by our lab,[40] we observed significant
195 variability in the number of MLF2-GFP foci/cells. However, all compounds significantly
196 reduced perinuclear MLF2-GFP accumulation at 2x and 8x their respective IC_{50}.
197 To ensure complete reduction of condensate markers, we tested the effect of
198 each drug on reducing the endogenous NE condensate biomarker, K48-linked ubiquitin
199 (K48), using slightly elevated concentrations. Our lab previously reported that 4TorKO
200 cells have reduced protein turnover, resulting in the accumulation of polyubiquitinated
201 proteins within NE condensates.[1,40] Using immunofluorescence staining with α-K48 anti-
202 bodies, all four compounds demonstrated a statistically significant decrease in endoge-
203 nous, perinuclear K48 foci in addition to MLF2-GFP (Figure 3B). Given the optimal con-
204 centration profile of PZ and celastrol (Figure 2D), we confirmed that each compound re-
205 sults in the redistribution of both MLF2-GFP and endogenous K48 foci using confocal
206 microscopy (Figure 3C). Importantly, this data validates that the mechanism of action
207 (MOA) either directly or indirectly mediates endogenous protein levels within conden-
208 sates, independent of the inducible MLF2-GFP biomarker system.

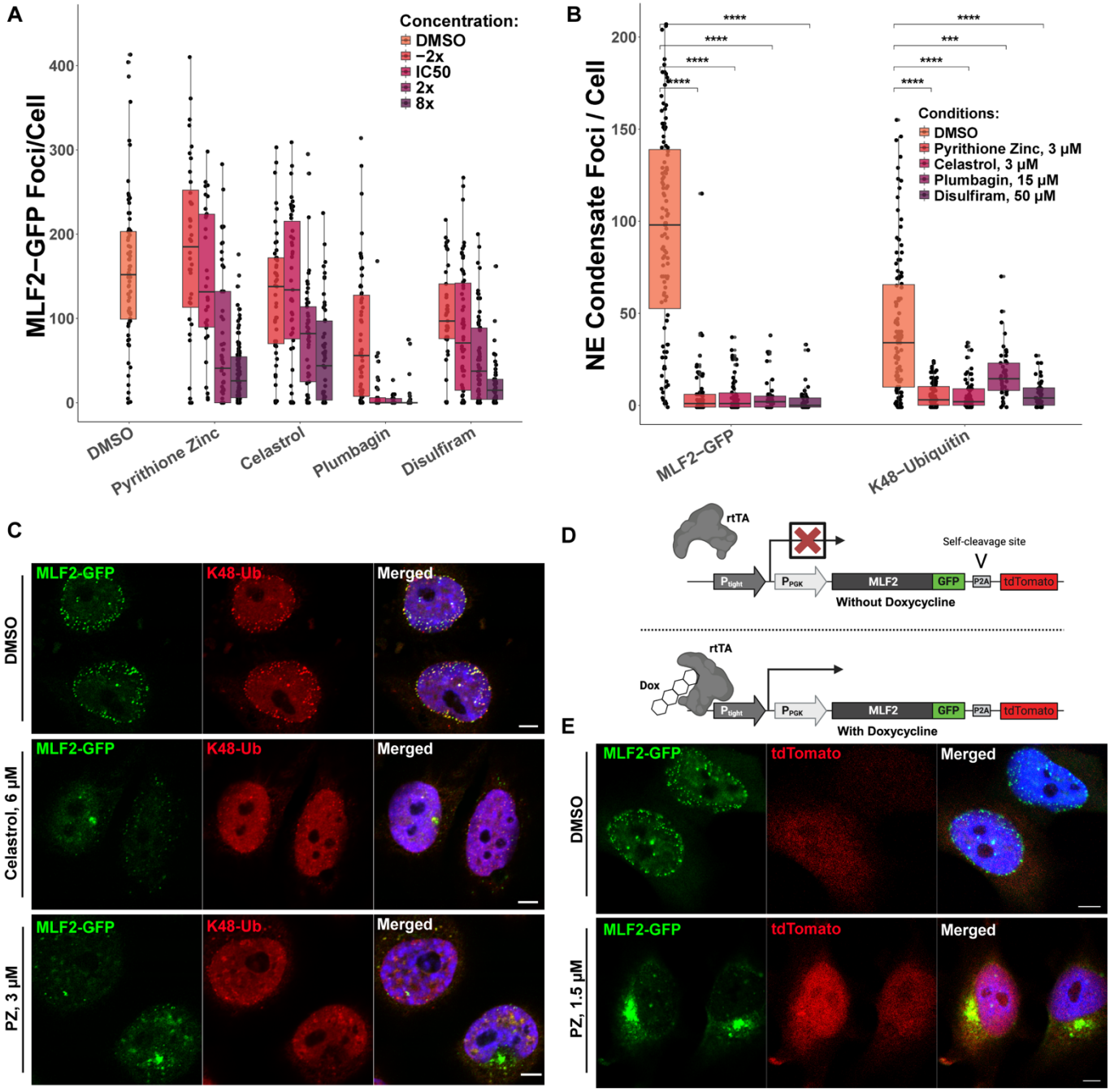

Fig. 3 | Four FDA-approved drugs decrease NE condensate markers in torsin-deficient cells. (A) Drug treatment decreases nuclear MLF2-GFP foci. Torsin-deficient cells expressing MLF2-GFP (8 h) were treated at four different concentrations (2x below IC_{50}, at IC_{50}, 2x above IC_{50}, and 8x above IC_{50}) for 3 h with either PZ, celastrol, plumbagin, or disulfiram. Nuclear MLF2-GFP foci were compared between treated and DMSO (orange boxplot) conditions. Each dot represents the number of MLF2-GFP foci for a single cell, while the horizontal lines indicate the median foci/condition. (B) Drugs modulate K48-Ub orthogonal NE condensate biomarker. Dots depict the number of MLF2-GFP foci (left, 6h Dox) and endogenous α-K48-ubiquitin (right) foci/cell after treatment with drug or DMSO. Asterisks indicate Bonferroni-corrected p-values determined by Mann-Whitney U testing (***: p <= 0.001 ****: p <= 0.0001). (C) Representative immunofluorescence confocal images of MLF2-GFP (green) and α-K48-ubiquitin (red) in torsin-deficient cells treated with DMSO compared to either PZ (3 μM) or celastrol (6 μM). (D) Schematic of inducible MLF2-GFP-P2A construct without (top) or with (bottom) Dox. (E) Confocal images of torsin-deficient cells expressing MLF2-GFP-P2A-tdTomato comparing DMSO or 1.5 μM PZ treatments (6h). Scale bars, 5 μm.

209

210 A significant limitation to phenotype screening efforts is the identification of false
211 positives that inhibit biomarker expression by non-specifically disrupting cellular protein
212 transcription or translation. To circumvent this, we designed a HeLa cell line with an in-
213 ducible bicistronic MLF2-GFP-P2A-tdTomato reporter (Figure 3D). The P2A site in-
214 duces ribosomal skipping, allowing the translation of a single open reading frame (ORF)
215 to yield two separate polypeptides: an N-terminal MLF2-GFP and a C-terminal
216 tdTomato, both derived from the same mRNA transcript.[62]
217 Furthermore, we developed an empirical metric, the Condensate Normalization
218 Score (CNS), to quantify the effects of candidate condensate modulators. The CNS is
219 calculated by comparing the reduction in the condensate biomarker (MLF2-GFP foci) to
220 the integrated fluorescent intensity of a secondary reporter (tdTomato), both normalized
221 to control conditions. A high CNS indicates compounds that effectively reduce conden-
222 sate biomarkers with minimal impact on overall protein expression. In contrast, a low
223 CNS suggests a non-specific or off-target effect such as decreased transcription, pro-
224 tein expression, or increased turnover.
225 After FACS sorting the MLF2-GFP-P2A-tdTomato 4TorKO HeLa cells (Figure
226 S1C), we induced MLF2-GFP expression and treated cells with either 0.75 μM/1.5 μM
227 of PZ or 1.5 μM/3 μM of celastrol for a total of 6 h. This was compared with either unin-
228 duced cells treated with DMSO vehicle control, induced cells treated with DMSO, and
229 induced cells treated with 100 μg/mL cycloheximide. Concentrations of both celastrol
230 and PZ at 1.5 μM had a significant decrease in the number of MLF2-GFP foci/cell com-
231 pared with the DMSO control (Figure S1D). While PZ did not reduce the expression of
232 secondary-tdTomato reporter, celastrol slightly, albeit at a non-statistically significant
233 level, decreased secondary reporter expression compared with DMSO-treated cells
234 (Figure S1E). After normalizing to the DMSO control, both celastrol and PZ-treated cells
235 had a significantly increased median condensate normalization score (CNS) (Figure
236 S1F) compared to all controls, indicating a mechanism of action (MOA) independent of
237 altered global protein expression. However, visualization of condensates in 4TorKO
238 cells using transmission electron microscopy (TEM) did not reveal full dissolution of NE
239 condensates after a 3 h treatment of 2 μM PZ (Figure S1G). Further testing of additional

concentrations and time points may reveal differential kinetics between condensate resolution compared to modulation of condensate content (MLF2/K48-Ub-proteins).

Despite lack of complete NE condensate resolution, both celastrol and PZ treatment lead to the redistribution of endogenous K48 NE condensate biomarkers (Figures 3B, 3C). Given the short incubation period (3 h) and the high half-life of proteins within NE condensates,[1] it is very unlikely that either compound significantly alters the concentration of endogenous condensate proteins solely by reduced protein expression. Collectively, these findings strongly suggest that these drugs operate through a mechanism independent of differential protein expression. Importantly, our small-scale screening effort serves as proof of concept and motivates additional screening efforts.

Whole-Genome CRISPR Screen Reveals Key Autophagy, Cell Division, and Protein Transport Pathways in Condensate Modulation

Identifying proteins involved in protecting cells from aberrant condensate formation has direct therapeutic potential for diseases such as ALS, FTD, and dystonia. To determine genes safeguarding against aberrant condensate formation, we completed a genome-wide CRISPR/Cas9 knock-out (KO) screen in WT HeLa cells using our established high-content imaging platform with MLF2-GFP as a condensate biomarker. We screened the Horizon Discovery Edit-R synthetic sgRNA library, which is an arrayed library targeting 19,195 human genes comprising Drug Targets, Druggable Genome, and Human Genome libraries.

To increase KO efficiency, we designed and FACS-sorted a WT HeLa cell line that constitutively expresses Cas9 with Dox-inducible MLF2-GFP. Each well was reverse-transfected in a 384-well plate format using a pool of 3 sgRNAs targeting different regions of the same gene (Figure 4A). Cells were incubated for 72 h, and MLF2-GFP was induced with Dox 16 h before fixation. After running all high-content images through our *CondenScreen* pipeline, the average Z' value was 0.52, demonstrating a dynamic range between the positive (TOR1A/B sgRNAs) and negative (non-targeting (NT) sgRNA) controls. The calculated SB was 4.9, and the SD and CV of the NT control were 3.1 and 9.7, respectively. We determined the assay quality score to be sufficiently robust as indicated by similar scores in the literature.[51,63]

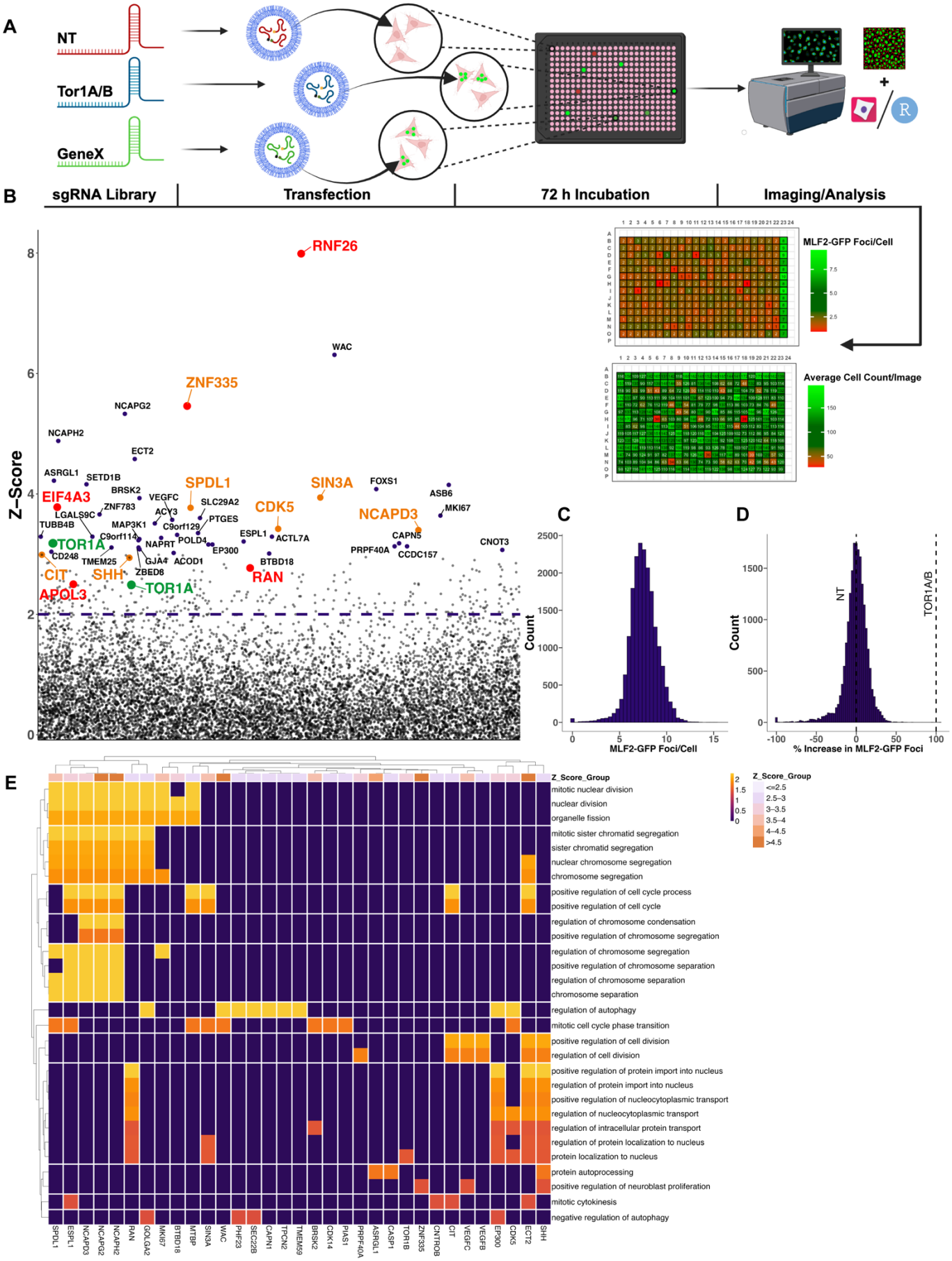
A
NT
Tor1A/B
GeneX
B
sgRNA Library
Transfection
72 h Incubation
Imaging/Analysis
MLF2-GFP Foci/Cell
Average Cell Count/Image
Z–Score
RNF26
WAC
ZNF335
NCAPG2
NCAPH2
ECT2
ASRGL1
SETD1B
BRSK2
VEGFC
SPDL1
SIN3A
FOXS1
ASB6
EIF4A3
ZNF783
SLC29A2
CDK5
MKI67
LGALS9C
ACY3
PTGES
NCAPD3
TUBB4B
MAP3K1
C9orf129
C9orf114
POLD4
ESPL1
ACTL7A
CAPN5
CNOT3
TOR1A
NAPRT
EP300
PRPF40A
CCDC157
CD248
TMEM25
GJA4
ACOD1
BTBD18
CIT
SHH
ZBED8
RAN
TOR1A
APOL3
C
Count
MLF2-GFP Foci/Cell
D
Count
NT
TOR1A/B
% Increase in MLF2-GFP Foci
E
Z_Score_Group
mitotic nuclear division
nuclear division
organelle fission
mitotic sister chromatid segregation
sister chromatid segregation
nuclear chromosome segregation
chromosome segregation
positive regulation of cell cycle process
positive regulation of cell cycle
regulation of chromosome condensation
positive regulation of chromosome segregation
regulation of chromosome segregation
positive regulation of chromosome separation
regulation of chromosome separation
chromosome separation
regulation of autophagy
mitotic cell cycle phase transition
positive regulation of cell division
regulation of cell division
positive regulation of protein import into nucleus
regulation of protein import into nucleus
positive regulation of nucleocytoplasmic transport
regulation of nucleocytoplasmic transport
regulation of intracellular protein transport
regulation of protein localization to nucleus
protein localization to nucleus
protein autoprocessing
positive regulation of neuroblast proliferation
mitotic cytokinesis
negative regulation of autophagy
SPDL1
ESPL1
NCAPD3
NCAPG2
NCAPH2
RAN
GOLGA2
MKI67
BTBD18
MTBP
SIN3A
WAC
PHF23
SEC22B
CAPN1
TPCN2
TMEM59
BRSK2
CDK14
PIAS1
PRPF40A
ASRGL1
CASP1
TOR1B
ZNF335
CNTROB
CIT
VEGFC
VEGFB
EP300
CDK5
ECT2
SHH
<=2.5
2.5–3
3–3.5
3.5–4
4–4.5
>4.5

Fig. 4 | Identification of genes that safeguard against NE condensates. (A) Schematic workflow of the genome-wide CRISPR KO screen in WT HeLa cells. Representative output plates indicating the number of MLF2-foci/cell (top plate) and cell count per image (bottom plate). (B) Scatter plot of candidate genes after CRISPR KO. A significance threshold was set (Z-score > 2, dotted line) and compounds surpassing a Z-score > 3 are highlighted in purple. Red dots indicate genes of great interest; green dots represent the TorsinA and TorsinB KO conditions; orange dots represent genes linked to microcephaly. (C) Histogram of the average MLF2-GFP foci/cell distribution for each KO condition. (D) Histogram of the percent increase in MLF2-GFP foci/cell normalized to the average across the screening population. (E) Heatmap of the 30 highest-scoring biological processes (rows) and associated genes (columns) from the top 100 candidate genes. GO analysis compared enriched CRISPR candidate genes against the org.Hs.eg.db gene set. Color scale legend indicates -log(10) Benjamini-Hochberg adjusted p-value, with lighter regions representing higher significance. Scaled boxes at top indicate each gene's significance (Z-score), with darker orange indicating a higher Z-score. Euclidean distance hierarchical clustering for GO-enriched biological pathways and genes is shown with the left and top dendrogram, respectively.

We defined a candidate gene as any gene deletion that resulted in a Z-score > 2 (Figure 4B). The top 10-ranked candidate genes were: RNF26, WAC, ZNF335, NCAPG2, NCAPH2, ECT2, ASRGL1, SETD1B, ASB6, and FOXS1. The entire ranked list of screened genes can be found in the supplementary materials (Table S2). Overall, the screen resulted in a near-normal distribution of the average number of MLF2-GFP foci per cell (Figures 4C, 4D). Notably, among these hits, we observed several genes linked to neurodevelopmental disorders, with especially high enrichment of microcephaly-associated genes (orange, Figure 4B), including ZNF335.[64,65]

As defects in lipid metabolism and nucleocytoplasmic transport have been linked to torsin-deficiency,[28,66,67] three additional candidate genes of interest include APOL3 (Z-score = 2.5), a putative regulator of membrane dynamics with detergent-like bactericidal properties,[68,69] and the GTP-binding nuclear protein, Ran (Z-score = 2.8), and Nup50 (Z-score = 2.5), associated with NPC biogenesis and ALS/FTD. [70,71] Additionally, a high percentage of the Condensin-2 complex (NCAPG2, NCAPH2, NCAPD3, and SMC2) indicates a potential role of either liquid-like condensates or MLF2 in chromosomal condensation. Recently, DEAD-box ATPases have been linked to the regulation of phase-separated membranelles organelles.[72] A key DEAD-box RNA helicase, EIF4A3 (also known as DDX48, Z-score = 3.8), scored as a top candidate gene, indicating a potential novel role of EIF4A3 in modulating phase transitions. The condensate phenotypes of each gene deletion condition represent areas where future research is warranted.

To determine if candidate genes are clustered into enriched genetic pathways, we grouped the top 100 gene hits (< top 1% of screen hits) and hierarchically clustered the top 30 enriched biological processes (q-value < 0.05) using GO analysis (Figure 4E; interactive webpage available on CondenScreen GitHub:

297 https://github.com/SchliekerLab/Condenscreen-v1.1/tree/main/Interactive%20Figures)
298 and illustrated pathway interconnectedness (Figure S2A). Groups were delineated using
299 unsupervised machine learning clustering (*pheatmap*, *R*, Figure 4E), before being man-
300 ually clustered into the following five categories: Autophagy, Cell Cycle, Chromosomal
301 Regulation, Protein Transport, and Other (Figure S2B). Each enriched pathway was
302 mapped to its corresponding genes (Figure S2C). Consistent with these enriched path-
303 ways, loss of protein homeostasis,[1,73] a cell-cycle dependency of condensates,[40] and
304 disruption to nucleocytoplasmic transport[28,44] have all been documented in DYT1 dysto-
305 nia models. Beyond the enrichment of individual gene hits linked to microcephaly, en-
306 cephalopathies, and other neurodevelopmental disorders, additional enriched pathways
307 of interest included organelle fission and positive regulation of neuroblast proliferation.
308

309 **RNF26 but not ZNF335 Condensates Co-localize with Nucleoporin Marker**

310 Among candidate genes, RNF26 (Z-score = 8.0) and ZNF335 (Z-score 5.5) stood out
311 due to their high significance. Of interest, RNF26 (RING finger protein 26) is an E3-ubiq-
312 uitin ligase that has been implicated in the integral regulation of the endosomal system,
313 serving as a “gatekeeper” for vesicles in the perinuclear ER cloud.[74,75] Furthermore, it
314 ubiquitinates SQSTM1[74] and has recently been tied to ER-sheet morphology and
315 maintenance.[75] ZNF335 (zinc finger protein 335) has been tied to neurogenesis, micro-
316 cephaly, and potentially modulation of cholesterol.[76–81] The AlphaFold 3 (AF)[82] structure
317 for ZNF335 predicts high intrinsic disorder along with 13-C2H2 zinc finger domains (Al-
318 phaFold model: AF-Q9H4Z2-F1-v4). However, the predicted structure is of low confi-
319 dence with a high number of pLDDT regions <50.

320 As it is known that torsin-deficient cells form perinuclear condensates within
321 omega-shaped membrane herniations[32,41], we investigated whether RNF26 and
322 ZNF335-deficient cells shared a similar phenotype. To determine potential co-localiza-
323 tion with NPC-localized FG-nups, we performed immunofluorescence staining using α-
324 mAb414, which detects Nup62, Nup153, Nup214, and Nup358. To our surprise, RNF26
325 KO HeLa cells showed prominent MLF2-GFP co-localization with mAb414, similar to
326 condensates linked with stalled NPCs found in torsin-deficient cells (Figure 5A). In con-
327 trast, analysis of confocal Z-stacks revealed that condensates in ZNF335 KO cells

328 rarely shared significant co-localization with mAb414 staining (Figure 5A, 5B). Both
329 RNF26 and ZNF335 KO cells accumulated K48-ubiquitin within their condensates, anal-
330 ogous to torsin-deficient cells as determined by expression of MLF2-GFP and K48-Ub
331 immunostaining (Figure 5C).
332 We deleted the three highest candidate genes, RNF26, ZNF335, and the WW
333 Domain Containing Adaptor With Coiled-Coil (WAC), and binned them according to the
334 number of nuclear MLF2-GFP foci/cell (5-15, 15-30, or >30 foci/cell) (Figure 5D).
335 RNF26 KO and ZNF335 KO cells displayed pronounced increases in nuclear MLF2-
336 GFP, while WAC depletion had only a modest effect. It should be noted that we consist-
337 ently documented mild background MLF2-GFP foci across NT-treated conditions, possi-
338 bly due to stress caused by the NT sgRNA or transfection reagents; however, all screen
339 results were normalized to account for this observation.
340 To test if MLF2-GFP accumulation represents condensates rather than aggre-
341 gates, we exposed cells with depletions of RNF26, ZNF335, and TOR1A/B to 1,6-hex-
342 anediol, a common reagent known to non-specifically disrupt liquid-liquid phase separa-
343 tion events.[83] Indeed, 1,6-hexanediol, but not 2,5-hexanediol, dissolved all three types
344 of condensates (Figure S3A). Strikingly, and consistent with immunofluorescence data,
345 TEM imaging demonstrated RNF26 KO cells contain condensates between the NE simi-
346 lar to those found in torsin-deficient cells using TEM (Figure 5E, shaded yellow). Addi-
347 tionally, RNF26 KO cells feature pronounced NE invaginations analogous to nucleoplas-
348 mic reticulum formation (Figure 5E).[84,85] While we observed several NE invaginations
349 contiguous with the inner nuclear membrane (INM), further electron tomographic studies
350 are needed to determine if all invaginations are contiguous with the NE. Together, these
351 results indicate that while both RNF26 and ZNF335 have a direct or indirect role in safe-
352 guarding against aberrant condensate formation, only RNF26 may be implicated in NPC
353 biogenesis or NE/NPC homeostasis.

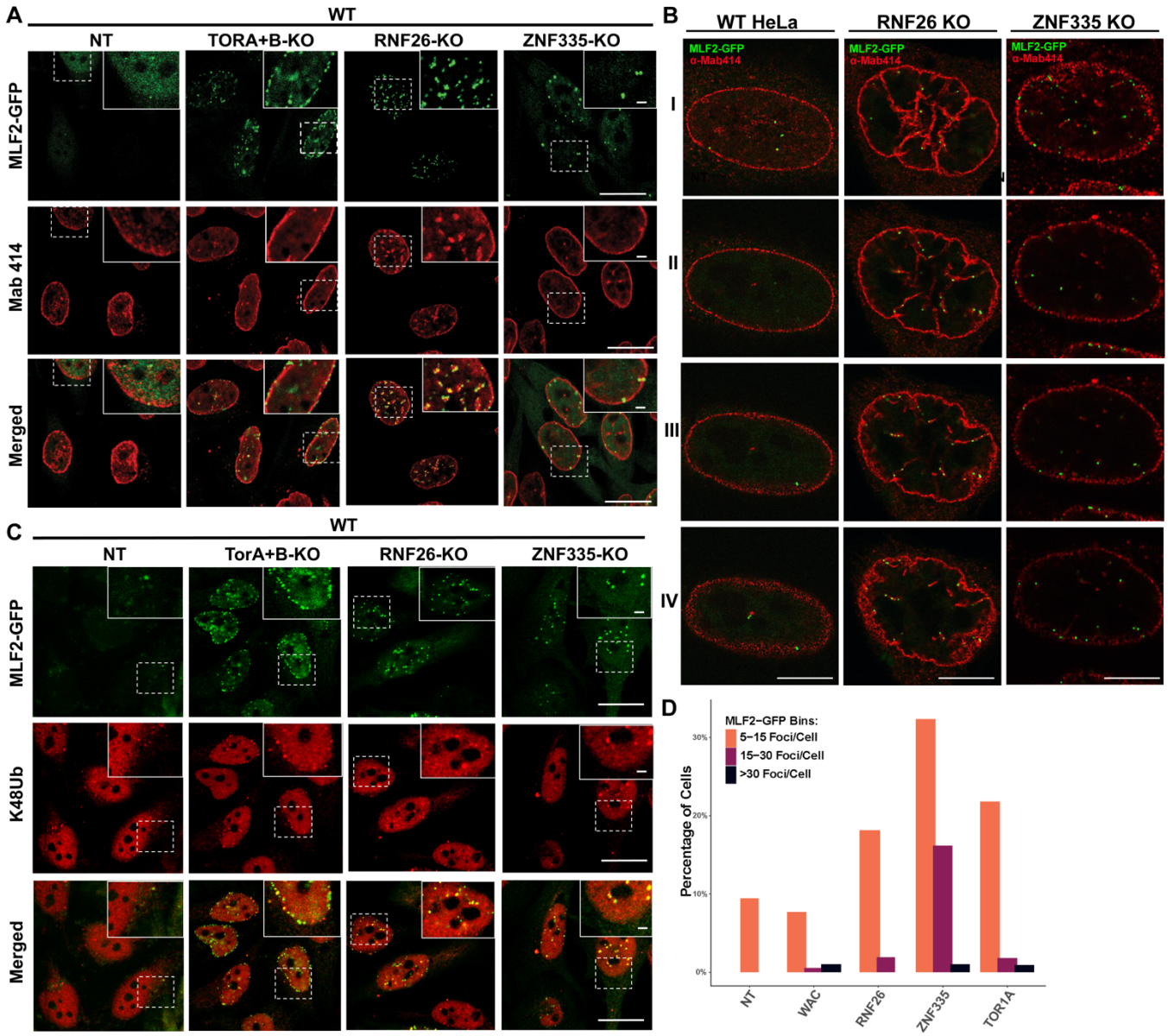
A
WT
NT
TORA+B-KO
RNF26-KO
ZNF335-KO
MLF2-GFP
Mab 414
Merged
B
WT HeLa
RNF26 KO
ZNF335 KO
MLF2-GFP
α-Mab414
I
II
III
IV
C
WT
NT
TorA+B-KO
RNF26-KO
ZNF335-KO
MLF2-GFP
K48Ub
Merged
D
MLF2−GFP Bins:
5−15 Foci/Cell
15−30 Foci/Cell
>30 Foci/Cell
Percentage of Cells
30%
20%
10%
0%
NT
WAC
RNF26
ZNF335
TOR1A

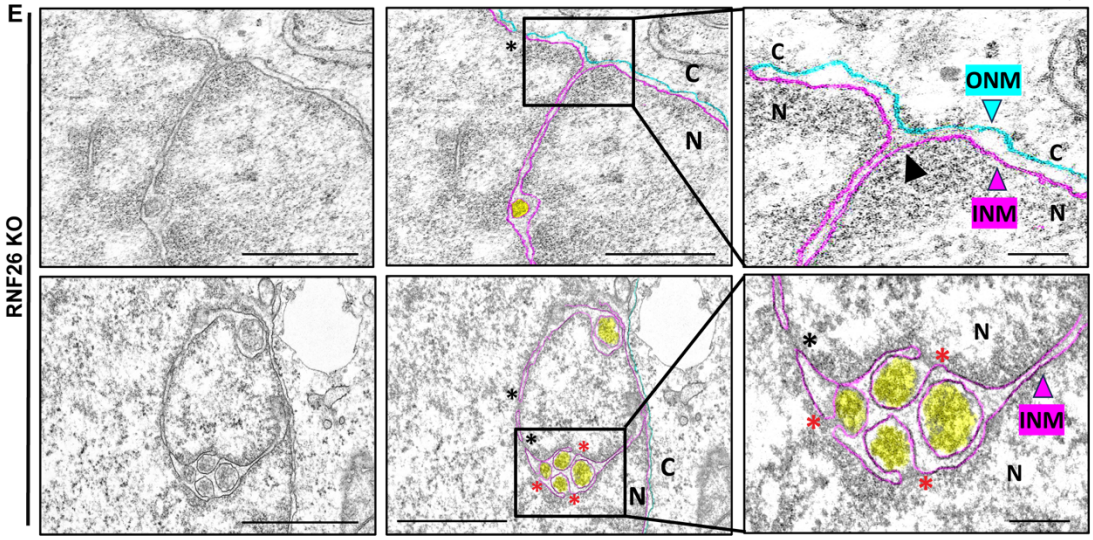
E
RNF26 KO
C
N
ONM
INM

Fig. 5 | RNF26 KO and ZN335 KO result in nuclear condensate formation. (A) A higher number of condensates from RNF KO compared to ZNF335 KO cells co-localize with NPC marker. Representative confocal immunofluorescence images of Cas9-integrated WT HeLa cells transfected with either (from left to right) NT, dual TOR1A + TOR1B, RNF26, or ZNF335 sgRNAs. Condensates are visualized using Dox-inducible MLF2-GFP (green) and stained with α-Mab414 antibody (red) to determine co-localization (yellow). (B) Z-stack projections of cells treated with the same conditions as (A). (C) RNF26 KO and ZNF335 KO condensates co-localize with K48-Ubiquitin. Immunofluorescence images comparing co-localization of MLF2-GFP (green) with α-K48-Ubiquitin staining (red). (D) Binned quantification of the number of MLF2-GFP foci after CRISPR KO of select candidate genes. RNF26 KO, ZNF335 KO, and WAC KO HeLa cells were compared against NT control. Bars indicate percent of cells with 5-15 foci MLF2-GFP foci/cell (orange), 15-30 foci (purple), or >30 foci (black). (E) TEM images of RNF26 KO cells depicting pronounced nuclear invaginations. Condensates are shaded yellow, while the INM and ONM are outlined in magenta and cyan, respectively. Black arrows draw attention to the interconnectedness of finger-like nuclear protrusions with INM; black asterisks indicate putative NPCs; red asterisks indicate omega-shaped herniations N, nucleus; C, cytoplasm; IF scale bars at 10 μm (main) and 2 μm (inset); EM scale bars at 250 nm (main) and 100 nm (inset).

354

355 **Microcephaly Disease Alleles of ZNF335 Fail to Fully Rescue Condensate Accu-**
356 **mulation.**

357 Seven out of the top 50 gene hits have been linked to microcephaly, including
358 ZNF335.[86,87] Genetic studies identified several hypomorphic ZNF335 mutations in mi-
359 crocephaly patients. Two mutations leading to severe microcephaly, p.Cys467Arg and
360 p.Arg1111His, result in either structural disruption of a conserved C2H2 zinc finger motif
361 or altered amino acid composition combined with defects in the 5' splice site within the
362 13th predicted zinc finger domain, respectively (Figure 6A).[65,77,78] We expressed cDNA-
363 HA constructs of ZNF335 with each of these mutations in ZNF335 KO HeLa cells to test
364 their ability to rescue condensate accumulation relative to WT ZNF335. As determined
365 using immunostaining against the ZNF335-HA cDNA constructs, overexpression of WT
366 ZNF335, but not either of the microcephaly-associated mutants, rescued the ZNF335
367 deletion by reducing the number of condensates to a level comparable to those ob-
368 served in WT HeLa cells transfected with NT sgRNAs (Figure 6B, 6C). Additionally, to
369 further validate the RNF26 KO, we overexpressed either WT RNF26 or an inactive mu-
370 tant p.Ile382Arg RNF26.[88] Only WT, but not the I382R mutation, of RNF26 fully rescued
371 condensate accumulation in RNF26 KO HeLa cells (Figure 6C, Figure S3B).

372

373 **Condensates in TOR1A, RNF26, and ZNF335-Deficient Cells are Modulated by Py-**
374 **rithione Zinc.**

375 As pyrithione zinc (PZ) was identified as a top hit from our small molecule screen, we
376 set out to differentiate whether the condensate modifying properties of PZ were due to
377 the pyrithione moiety (2-Mercaptopyridine N-oxide) or the zinc ion. To this end, we
378 treated 4TorKO HeLa cells with either DMSO vehicle control, PZ alone, or PZ with zinc

379 chelator TPEN (N,N,N',N'- *tetrakis*-(2-Pyridylmethyl)ethylenediamine) at a 3 molar
380 equivalent.[89] After zinc chelation with TPEN, the pyrithione compound did not reduce
381 MLF2-GFP condensate accumulation in 4TorKO cells (Figure 6D). Treatment with
382 TPEN alone resulted in increased cytosolic MLF2-GFP accumulation (Figure 6D). Fur-
383 thermore, we tested whether zinc alone is sufficient to deplete nuclear MLF2-GFP con-
384 densate foci. Due to the lower membrane permeability, 4TorKO cells were treated with
385 high concentrations of zinc sulfate monohydrate ($ZnSO_4$); studies indicate greater than
386 a 50- to 500-fold molar excess of $ZnSO_4$ may be needed to have the same effect as
387 PZ.[90,91] Treatment with 2 mM $ZnSO_4$ alone resulted in a robust decrease in MLF2-GFP
388 foci (Figure S4A, S4B) while maintaining tdTomato expression (Figure S4C), resulting in
389 a high CNS value (Figure 6E).
390 Finally, since PZ demonstrated a potent ability to modulate the MLF2-GFP con-
391 densate marker in torsin-deficient cells, we tested whether it could similarly modulate
392 NE condensates in RNF26 KO and ZNF335 KO cells. In both KO conditions, treatment
393 with 2 μM PZ significantly reduced nuclear condensate formation as marked by MLF2-
394 GFP accumulation (Figure 6F, 6G). These data indicate that PZ works in a zinc-depend-
395 ent manner and acts as a potent modulator of condensate formation in RNF26 KO and
396 ZNF335 KO cells, as well as in the pathological NE condensates of torsin-deficient cells
397 associated with DYT1 dystonia.

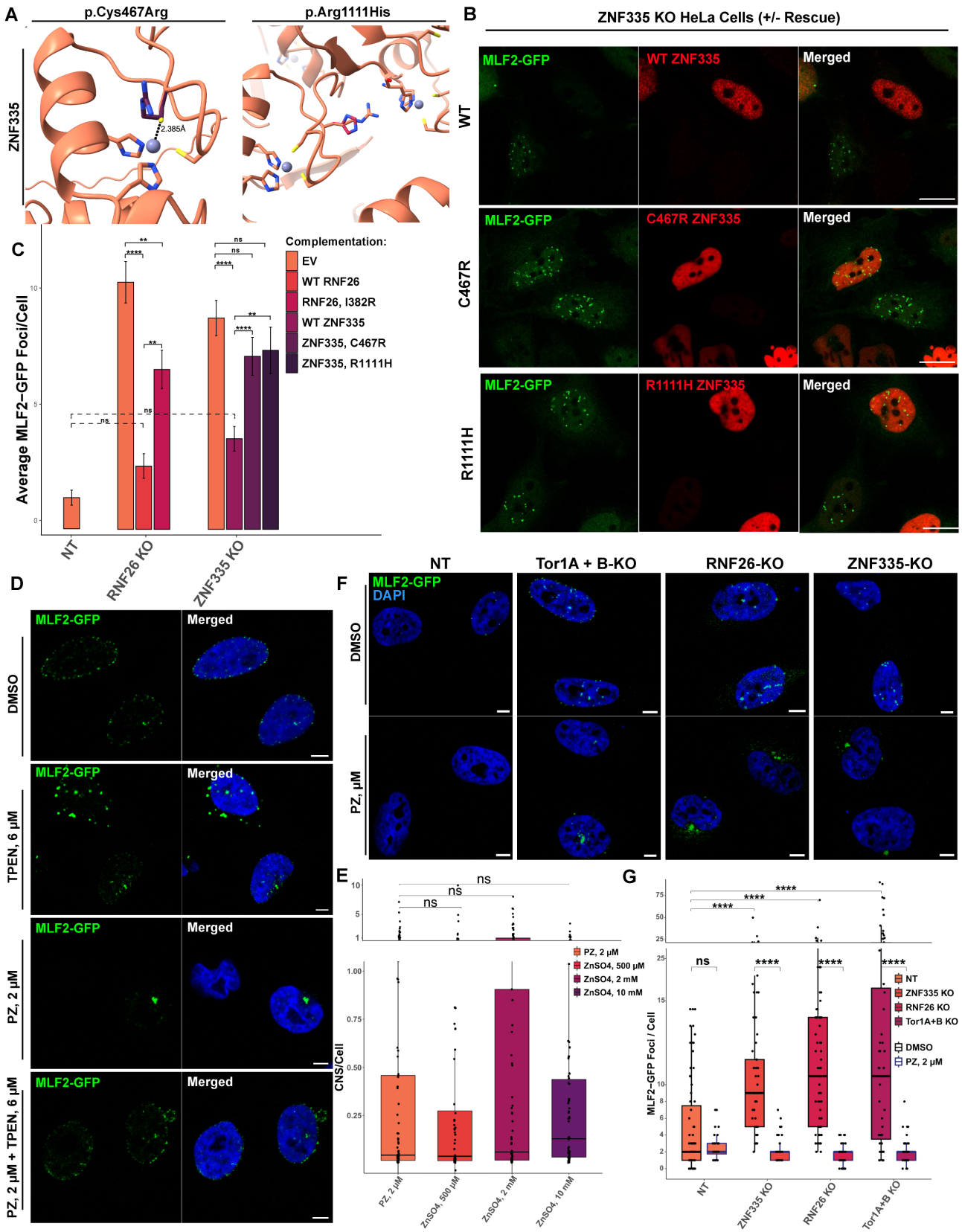
A
p.Cys467Arg
p.Arg1111His
ZNF335
2.385Å
B
ZNF335 KO HeLa Cells (+/- Rescue)
WT
C467R
R1111H
MLF2-GFP
WT ZNF335
C467R ZNF335
R1111H ZNF335
Merged
C
Average MLF2−GFP Foci/Cell
Complementation:
EV
WT RNF26
RNF26, I382R
WT ZNF335
ZNF335, C467R
ZNF335, R1111H
NT
RNF26 KO
ZNF335 KO
D
DMSO
TPEN, 6 μM
PZ, 2 μM
PZ, 2 μM + TPEN, 6 μM
MLF2-GFP
Merged
F
NT
Tor1A + B-KO
RNF26-KO
ZNF335-KO
DAPI
PZ, μM
E
CNS/Cell
PZ, 2 μM
ZnSO4, 500 μM
ZnSO4, 2 mM
ZnSO4, 10 mM
G
MLF2−GFP Foci / Cell
NT
ZNF335 KO
RNF26 KO
Tor1A+B KO
DMSO
PZ, 2 μM

398

Fig. 6 | Condensate rescue is impaired by microcephaly mutations but modulated by pyrithione zinc. (A) Structural representation of ZNF335 with two microcephaly patient disease alleles. The p.Cys467Arg mutation (left image, purple residue) disrupts the second conserved C2H2 zinc finger motif of ZNF335. The p.Arg1111His mutation (right image, red residue) results in splicing defects. (B) Only WT ZNF335 rescues the condensate formation of ZNF335 KO cells. Hela cells with a ZNF335 KO were transfected with either WT ZNF335-HA, C467R ZNF335-HA, or R1111H ZNF335-HA. Cells were immunostained against HA (red), and MLF2-GFP was used as a condensate marker. (C) Quantification comparing rescue of WT vs hypomorphic alleles for ZNF335 KO and RNF26 KO cells. HeLa cells were transfected with either non-targeting (NT), RNF26, or ZNF335 sgRNAs before attempted rescue with empty vector control (EV), WT, or associated loss-of-function alleles. See (B) and Figure S3B for representative ZNF335 KO and RNF26 KO immunofluorescence images, respectively. (D) TPEN negates the effect of PZ treatment. Confocal images of 4TorKO cells expressing MLF2-GFP (green) and stained with Hoechst (nucleus, blue). Cells were treated with either DMSO, 6 μM TPEN, 2 μM PZ, or 6 μM TPEN + 2 μM PZ (3 h). Scale bar, 5 μm. (E) Zinc sulfate is sufficient for condensate modulation. Quantification indicates no statistically significant difference between the CNS-value of 4TorKO treated with either 2 μM PZ, 500 μM ZnSO4, 2 mM ZnSO4, or 10 mM ZnSO4. Corresponding confocal images in Figure S4A. (F) PZ modulates condensates of RNF26 KO and ZNF335 KO cells. HeLa expressing MLF2-GFP (green) were treated with NT, Tor1A/B, RNF26, or ZNF335 sgRNAs and 2 μM PZ or DMSO for 3 h. Scale bar, 5 μM. (G) Quantification of MLF2-GFP foci in CRISPR KO cells after PZ treatment. Boxplots outlined in black or blue were treated with DMSO or 2 μM PZ, respectively. Asterisks indicate Bonferroni-corrected p-values by Mann-Whitney U testing (****: p <= 0.0001). Scale bars at 10 μm (6B) and 5 μm (6D,6F).

DISCUSSION

This study aimed to establish a high-throughput platform suitable for identifying small molecules and genes that modulate aberrant condensates, which have increasingly been linked to neurological disorders.[14,16,92] Starting with our established readout for aberrant condensates in a cell-based model for primary dystonia,[40] we validate our platform through the identification of compounds that tune key properties of aberrant phase transitions. We further exploited our platform to conduct a genome-wide CRISPR KO screen and identified a set of genes that recently emerged from sequencing patients suffering from dystonia and neurodevelopmental disorders, suggesting yet unappreciated commonalities in the cellular pathology underlying these conditions.[93,94] Given that deleting one of our top hits, ZNF335, previously linked to microcephaly,[64,65,77,79] induces nuclear condensates (Fig. 5) and that disease alleles fail to rescue this phenotype (Fig. 6 B, 6C), we suggest a role for aberrant nuclear condensate formation in microcephaly. To our knowledge, a link between microcephaly and aberrant condensation has not been reported. Thus, our study puts forward a list of genes tied to neurological disorders that deserve future scrutiny from the perspective of condensate biology, possible impairment of nuclear proteostasis, and potential drug targets.

A key advance from our results is the establishment of MLF2 as a robust and disease-agnostic marker for aberrant condensates. The known proclivity of MLF2 toward immersing into aberrant condensates[1] has enabled us to perform both pharmacological and genomic screening. Not only is MLF2 a primary biomarker for DYT1 dystonia-associated NE condensates, but MLF2 is also recruited to stress granules associated with

422 ALS/FTD, as demonstrated by its co-localization with TDP-43 and G3BP1 (Figure 1B).
423 Thus, our high-content imaging platform and *CondenScreen* analysis pipeline can be
424 readily adapted to support a range of condensate screening campaigns, even when the
425 affected disease allele product is not itself a condensate constituent, as exemplified by
426 Torsin or ZNF335 mutations, which induce aberrant condensates via indirect mecha-
427 nisms.[1,46]

428 Inspired by recent condensate-modifying (c-mod) campaigns,[51,52,95,96] we
429 screened for drugs that could modulate condensates either directly or indirectly. Several
430 of our identified drug hits caused robust re-localization of both expressed (MLF2-GFP)
431 and endogenous (K48-Ub) nuclear condensate markers (Figure 3C, 3E), without signifi-
432 cantly altering reporter expression. Divalent zinc influences the aggregation of TIA-1,[97]
433 stress granule formation,[97] liquid-liquid phase separation of tau,[98] and activation of au-
434 tophagy.[99] We found that pyrithione zinc acts through a divalent zinc-dependent mecha-
435 nism (Figure 6D), further indicating the importance of tight intracellular zinc in regulation
436 of phase transitions.

437 Additionally, celastrol, plumbagin, and disulfiram are all linked to increased au-
438 tophagy, oxidative stress, and inhibition of NF-κB activation.[100–107] Additionally, celastrol
439 has been linked to upregulation of the heat shock response and lipid metabolism.[108,109]
440 These data align with prior observations that impaired proteostasis and stress response
441 pathways, including the heat shock response, autophagy, and the integrated stress re-
442 sponse (ISR) pathway, are tied to protein aggregation and have been previously impli-
443 cated in DYT1 dystonia.[1,73,110–115] A recent screen identified ritonavir, an ISR inducer,
444 that restores the mislocalization of mutant TorsinA and abnormal physiological brain
445 readouts connected to dystonia.[116] Collectively, these findings exemplify the utility of our
446 platform to uncover both established and novel therapeutic pathways. Notably, a subset
447 of these compounds, including pyrithione zinc and disulfiram, was recently identified in
448 parallel efforts to modulate condensate linked to ALS,[52] underscoring that despite many
449 differences in disease onset and progression, shared etiological principles may never-
450 theless exist.

451 To identify cellular activities that are critical for modulating nuclear condensate
452 formation, we conducted a genome-wide CRISPR KO screen. Gene ontology analysis

453 indicated enrichment of gene hits clustered in pathways, including autophagy, protein
454 transport, chromosomal regulation, and cell cycle (Figure 2E, S2B). Key hits from these
455 pathways include ZNF335, RNF26, APOL3, NUP50, EIF4A3, and RAN. The top-scoring
456 hit, RNF26, was previously implicated in ER positioning, endosome retention, and
457 Sec62-mediated recovERphagy.[74,75,88] Cells deficient in RNF26 demonstrated colocali-
458 zation of MLF2-GFP condensates with FG-nups (Figure 5A, 5B), similar to condensates
459 associated with stalled NPCs seen in torsin-deficient cells.[32,41] Furthermore, RNF26-de-
460 ficient cells had abnormal nuclear envelope invaginations (Figure 5E) similar to those
461 found in torsin-deficient motor neurons derived from DYT1 dystonia patient iPSCs.[44]
462 Some NE invaginations share high similarity with canonical type 1 and type 2 nucleo-
463 plasmic reticulum,[84,85] warranting further EM analysis to assess NE connectivity. Given
464 RNF26's role in modulating autophagy via spatiotemporal control of endosomes,[74] and
465 the known or proposed involvement of autophagy in clearing nuclear pore complexes
466 (NPCs) and potentially nuclear aggregates,[117–120] further investigation is warranted to
467 determine whether RNF26 contributes to NPC biogenesis or their turnover through au-
468 tophagy.

469 A recent study investigated whole-exome sequencing from a large dystonia pa-
470 tient cohort (1,825 index patients).[94] Two dystonia patients from this cohort had disease
471 alleles of ZNF335 (c.1603C>T, c.3486_3487del), and one patient had a disease allele in
472 WAC (c.381+1G>T).[94] We discovered that depletion of ZNF335, a C2H2-type zinc fin-
473 ger protein highly expressed in the brain[76], results in nuclear condensate formation (Fig-
474 ure 5A-5D). Mutations or aberrant splice variants of ZNF335 result in severe microceph-
475 aly and, often, reduced life expectancy.[65,76–80] Moreover, knockdown of ZNF335 inhibits
476 neuronal differentiation and has been reported to regulate the REST/NRSF transcrip-
477 tional repressor.[65] In addition to ZNF335, pathogenic allelic variants of 15 out of the top
478 50 gene hits are associated with neurodevelopmental disorders according to human test
479 results from an Online Catalog of Human Genes and Genetic Disorders (OMIM)[86] and
480 the NIH Genetic Testing Registry (GTR)[87] (Figure 7, top panel). Strikingly, 7/15 of these
481 genes (ZNF335, SPDL1, NCAPD3, CDK5, SIN3A, SHH, and CIT) are linked to micro-
482 cephaly, holoprosencephaly, or lissencephaly (OMIM, GTR), along with additional find-
483 ings implicating NCAPG2, NCAPH2, and EP300 with microcephaly.[65,121–125]

Gene	Z-Score	Disorder	Gene	Z-Score	Disorder
RNF26	7.99	—	LGALS9C	3.29	—
WAC	6.31	Desanto-Shinawi Syndrome	NAPRT	3.27	—
ZNF335	5.46	Microcephaly	MAP3K1	3.25	46, XY sex reversal 6
NCAPG2	5.33	Khan-Khan-Katsanis Syndrome	C9orf114	3.23	Neurodevelopmental disorder with poor growth, seizures, and brain abnormalities
NCAPH2	4.88	Cardioencephalomyopathy, Myopia	ESPL1	3.21	—
ECT2	4.58	—	CAPN5	3.18	Vitreoretinopathy, neovascular inflammatory
ASRGL1	4.22	—	TOR1B	3.18	—
SETD1B	4.16	Intellectual Developmental Disorder with Seizures and Language Delay	POLD4	3.16	—
ASB6	4.15	—	EP300	3.16	Rubinstein-Taybi Syndrome 2, Menke-Hennekam Syndrome 2, Colorectal Cancer
FOXS1	4.08	—	PRPF40A	3.13	—
SIN3A	3.94	Witteveen-Kolk Syndrome (WITKOS)	CCDC157	3.13	—
BRSK2	3.93	Idiopathic Pulmonary Fibrosis Susceptibility*	ZBED8	3.11	—
EIF4A3	3.78	Robin Sequence with Cleft Mandible and Limb Anomalies	TMEM25	3.11	—
SPDL1	3.77	Severe Primary Microcephaly, Neonatal Death	GJA4	3.08	—
ZNF783	3.66	—	CNOT3	3.07	Intellectual developmental disorder with speech delay, autism, dysmorphic facies
MKI67	3.64	Long QT Syndrome	CD248	3.04	
SLC29A2	3.6	Bipolar disorder susceptibility*	ACOD1	3.02	Lymphatic Malformation
VEGFC	3.57	Lymphatic malformation	BTBD18	3.01	—
ACY3	3.51	—	CIT	2.99	Primary Microcephaly
CDK5	3.42	Isolated Microcephaly, Nonsyndromic Microcephaly, Lissencephaly	PHF23	2.99	—
NCAPD3	3.4	Primary Microcephaly	AK2	2.98	Reticular Dysgenesis
PTGES	3.35	—	TCEA2	2.98	—
C9orf129	3.32	—	C5orf60	2.95	—
TUBB4B	3.29	Leber Congenital Amaurosis with Early-Onset Deafness	SHH	2.94	Holoprosencephaly, Schizencephaly, Solitary Median Maxillary Central Incisor Syndrome, Microphthalmia
ACTL7A	3.29	Spermatogenic failure; breast cancer susceptibility*	LDLRAD1	2.93	—

Microcephaly/Congenital Brain Malformations	Other Neurodevelopmental Disorders	Cardiovascular, Lymphatic, Other	Ophthalmological Disorders

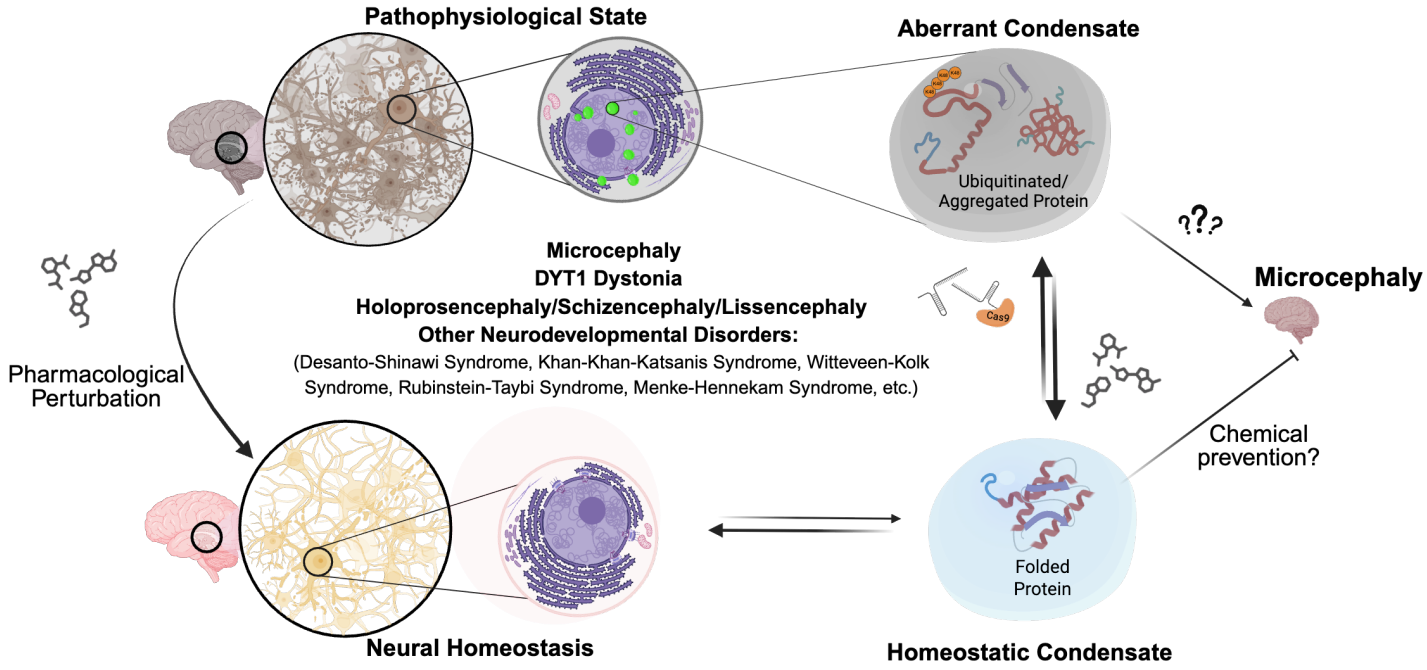

Fig. 7 | Targeting aberrant condensates as a therapeutic approach for neurodevelopmental disorders. (**top**) Candidate genes from CRISPR KO screen are implicated in neurodevelopmental disorders. Top 50 candidate genes (left columns), their significance score (Z-Score, middle columns), and associated diseases (right columns) are color-coded based on disorders. Rows labeled yellow indicate established link to microcephaly/congenital brain malformations, orange indicates other neurodevelopmental disorders, purple indicates ophthalmological disorders, and red indicates cardiovascular, lymphatic, or other disorders. Genes denoted with an asterisk indicate evidence from genome-wide association studies. Gene relevance to disease was determined based on allelic variants obtained from OMIM and GTR. (**bottom**) Schematic representation depicting the relationship between aberrant condensates and neurodevelopmental disorders. Genes involved in the etiology of primary microcephaly and encephalopathies were highly enriched, potentially indicating a role of condensate formation as a driver for these disorders. These condensates can be modulated using small molecules (such as pyrithione zinc and celastrol) or genetic perturbations. Targeting condensates could potentially lead to preserving neuronal homeostasis. Arrows indicate possible intervention points and potential outcomes.

Indeed, microcephaly-associated ZNF335 mutants failed to rescue nuclear condensates found in ZNF335-deficient cells (Figure 6B, 6C), suggesting a potential regulatory role of condensate formation driving microcephaly (Figure 7).

Several of the microcephaly-associated gene hits identified in our screen are also involved in chromosomal condensation, including several independently identified subunits of the condensin complex. Microcephaly has previously been labeled as a “condensinopathy”, not to be confused with condensatopathies, reflecting prior work that established a relationship between chromosomal condensation defects and reduced cerebral cortex size.[121] Thus, our work inspires future studies to explore the interplay between aberrant condensate formation and machinery normally involved in chromosomal regulation.

The insights gleaned from this chemical-genetic screening approach pave the way for a deeper mechanistic understanding and the exploration of novel therapeutic strategies targeting impaired proteostasis and altered phase transitions in dystonia, microcephaly, and related neurological disorders. As there is a paucity of generic phase-separation markers, this work identifies MLF2 as a versatile and novel disease-agnostic biomarker and reports several chemical modulators of specific aberrant phase transitions. Limitations include compounds exhibiting high toxicity at longer incubation timepoints or higher concentrations. Nevertheless, this screen represents an optimal starting point toward the derivatization of structurally analogous compounds with lower toxicity profiles.

Beyond the implications for disease, our data may offer insights into fundamental nuclear organization processes, including transcriptional regulation. Recent work has demonstrated that transcriptional condensates, formed via phase separation mechanisms, orchestrate RNA polymerase II dynamics, 3D genome architecture, and

510 transcriptional regulation even in healthy cells.[126,127] Previous work showed that the *Dro-*
511 *sophila melanogaster* homolog of human myeloid leukemia factors (MLFs) associates
512 with chromatin and alters gene expression by modulating transcription factor stabil-
513 ity.[128,129] Our findings, linking MLF2 to condensin and aberrant condensates, lay the
514 groundwork for future studies aimed at uncovering the function of these poorly charac-
515 terized proteins.
516 While the role of condensates in microcephaly and related disorders remains to
517 be fully elucidated, the ability of pyrithione zinc to modulate nuclear condensates in
518 ZNF335 knockout cells suggests that a similar chemical-modulator screening approach
519 could be potentially leveraged to identify therapeutics for microcephaly. Our screening
520 platform and analysis pipeline can be rapidly repurposed to screen novel chemical
521 space for pharmacological therapeutics of alternative phase transitions, including stress
522 granules. In conclusion, this study provides a genetic framework that will aid in the iden-
523 tification of cellular pathology to rationalize previous and ongoing sequencing efforts of
524 patients and inspire future investigations aimed at restoring cellular proteostasis in dis-
525 eases driven by aberrant biomolecular condensates.
526

527 **SUPPLEMENTARY FIGURES**

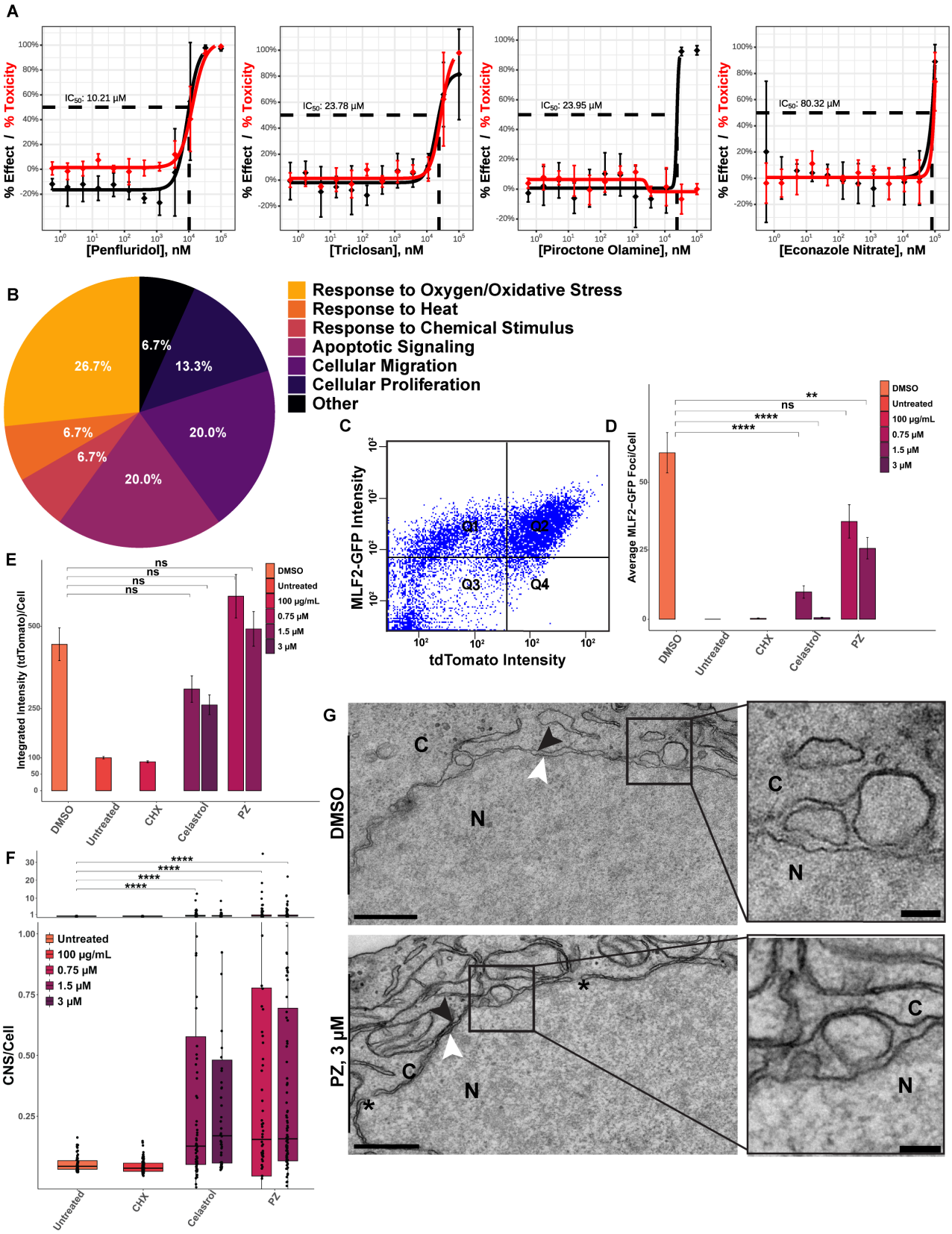

Figure S1. Validation of putative chemical hits from the Pharmakon 1760 screen. (A) Calculated IC_{50} values of additional compounds with a dose-dependent relationship. The black and red curves represent % effect and % toxicity relative to the DMSO control. The calculated IC_{50} values were extrapolated from a four-parameter-log-logistic model. (B) Manual clustering of GO biological pathways of chemical screen. High-confidence functional protein partners of chemical screen hits were analyzed using GO, and the statistically significant top 30 pathways were manually clustered within seven categories. Percentage indicates what fraction of the top 30 genes is associated with each cluster. (C) Distribution of FACS results for 4TorKO MLF2-GFP-P2A-tdTomato HeLa cell sorting. Cells within the upper-middle of quadrant 2 (Q2) were gated and sorted. Quantification of differences between the mean MLF2-GFP foci/cell (D) and tdTomato integrated intensity/cell (E) between untreated or DMSO, CHX, celastrol, or PZ treated 4TorKO cells. (F) Barplot of average CNS-values/cell across treatment conditions, normalized to the DMSO control. Higher CNS-values correspond with higher effect and lower repression against protein expression reporter (tdTomato). Asterisks indicate Bonferroni-corrected p-values determined by Mann-Whitney U testing (**: $p <= 0.01$; ***: $p <= 0.001$; ****: $p <= 0.0001$). (G) PZ does not result in complete NE condensate resolution despite modulation of condensate cargo. TEM images of 4TorKO HeLa cells treated with either 0.1% DMSO or 2 μM PZ for 3 h. Insets show NE condensates between the inner and outer nuclear envelopes. Scale bars at 500 nm; inset scale bars at 100 nm. Asterisk, putative nuclear pores; black arrowhead, outer nuclear envelope; white arrow, inner nuclear envelope; C, cytoplasm; N, nucleus.

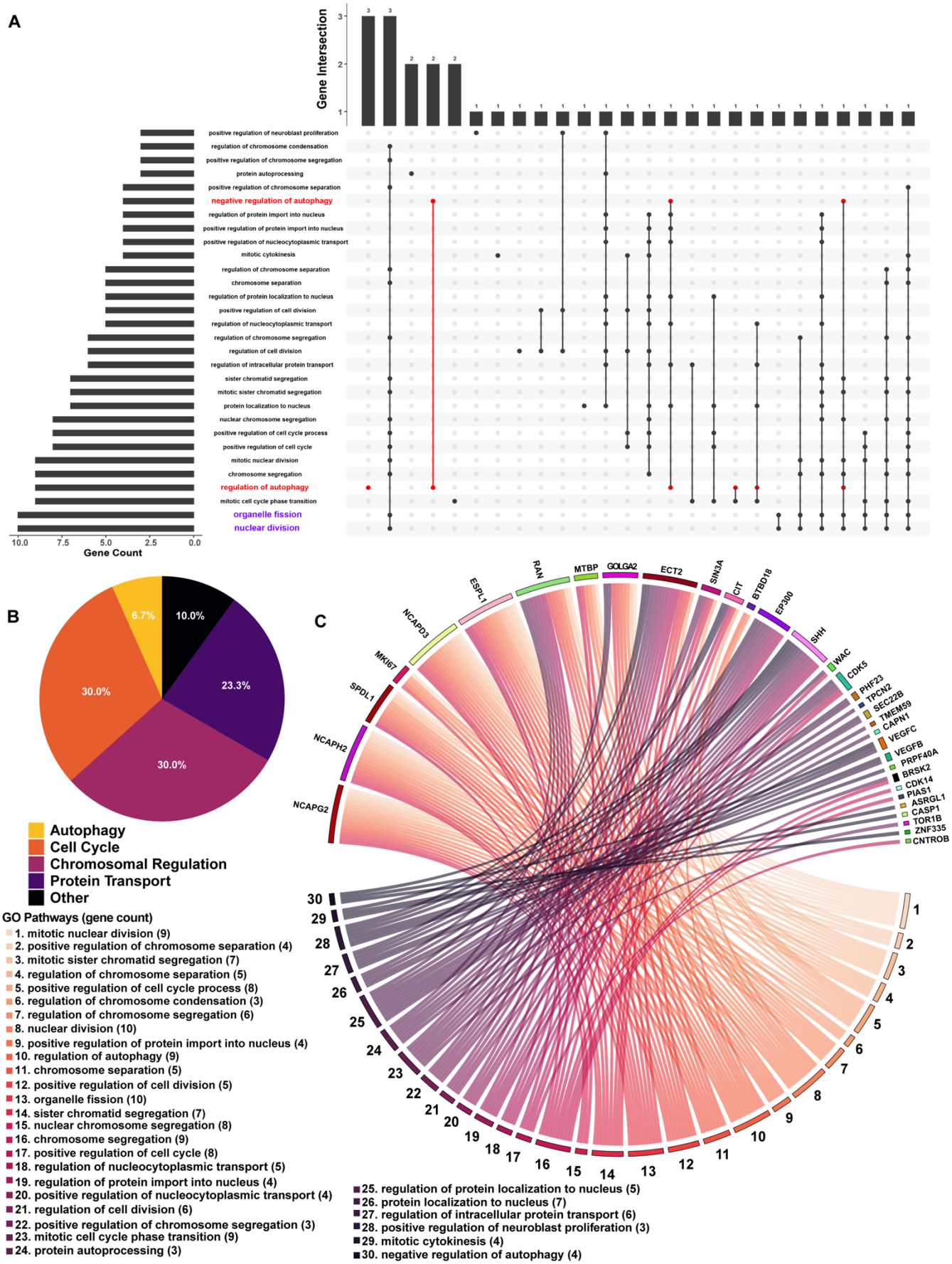
A
Gene Intersection
Gene Count
positive regulation of neuroblast proliferation
regulation of chromosome condensation
positive regulation of chromosome segregation
protein autoprocessing
positive regulation of chromosome separation
negative regulation of autophagy
regulation of protein import into nucleus
positive regulation of protein import into nucleus
positive regulation of nucleocytoplasmic transport
mitotic cytokinesis
regulation of chromosome separation
chromosome separation
regulation of protein localization to nucleus
positive regulation of cell division
regulation of nucleocytoplasmic transport
regulation of chromosome segregation
regulation of cell division
regulation of intracellular protein transport
sister chromatid segregation
mitotic sister chromatid segregation
protein localization to nucleus
nuclear chromosome segregation
positive regulation of cell cycle process
positive regulation of cell cycle
mitotic nuclear division
chromosome segregation
regulation of autophagy
mitotic cell cycle phase transition
organelle fission
nuclear division
B
6.7%
10.0%
30.0%
23.3%
30.0%
Autophagy
Cell Cycle
Chromosomal Regulation
Protein Transport
Other
C
NCAPD3
ESPL1
RAN
MTBP
GOLGA2
ECT2
SIN3A
CIT
BTBD18
EP300
SHH
WAC
CDK5
PHF23
TPCN2
SEC22B
TMEM59
CAPN1
VEGFC
VEGFB
PRPF40A
BRSK2
CDK14
PIAS1
ASRGL1
CASP1
TOR1B
ZNF335
CNTROB
MKI67
SPDL1
NCAPH2
NCAPG2
GO Pathways (gene count)
1. mitotic nuclear division (9)
2. positive regulation of chromosome separation (4)
3. mitotic sister chromatid segregation (7)
4. regulation of chromosome separation (5)
5. positive regulation of cell cycle process (8)
6. regulation of chromosome condensation (3)
7. regulation of chromosome segregation (6)
8. nuclear division (10)
9. positive regulation of protein import into nucleus (4)
10. regulation of autophagy (9)
11. chromosome separation (5)
12. positive regulation of cell division (5)
13. organelle fission (10)
14. sister chromatid segregation (7)
15. nuclear chromosome segregation (8)
16. chromosome segregation (9)
17. positive regulation of cell cycle (8)
18. regulation of nucleocytoplasmic transport (5)
19. regulation of protein import into nucleus (4)
20. positive regulation of nucleocytoplasmic transport (4)
21. regulation of cell division (6)
22. positive regulation of chromosome segregation (3)
23. mitotic cell cycle phase transition (9)
24. protein autoprocessing (3)
25. regulation of protein localization to nucleus (5)
26. protein localization to nucleus (7)
27. regulation of intracellular protein transport (6)
28. positive regulation of neuroblast proliferation (3)
29. mitotic cytokinesis (4)
30. negative regulation of autophagy (4)

Figure S2. Enriched gene pathways of candidate hits that promote NE condensate formation. (A) Upset plot depicting relationships between the top 30 GO-enriched biological process pathways. Horizontal bars (left) indicate the number of genes for each GO pathway, with terms ranked by gene count. Vertical bars (top) indicate the size of each intersecting gene set, representing the number of genes shared among multiple GO terms. The dot matrix below indicates shared genes among the corresponding GO terms (black dots connected by black line); single dots represent GO terms with unique gene sets. Red dots highlight autophagy-related pathways. (B) Manual clustering of GO biological pathways from the genome-wide KO screen in WT HeLa. The top 30 statistically significantly enriched for in the highest scoring 100 candidate genes were manually clustered within seven categories. Percentage indicates the fraction of genes within the top 30 pathways associated with each cluster. (B) Chord diagram mapping genes to GO terms. Each gene (outer labels, top) is linked to its corresponding GO terms (outer labels, bottom), with colored ribbons indicating relationships.

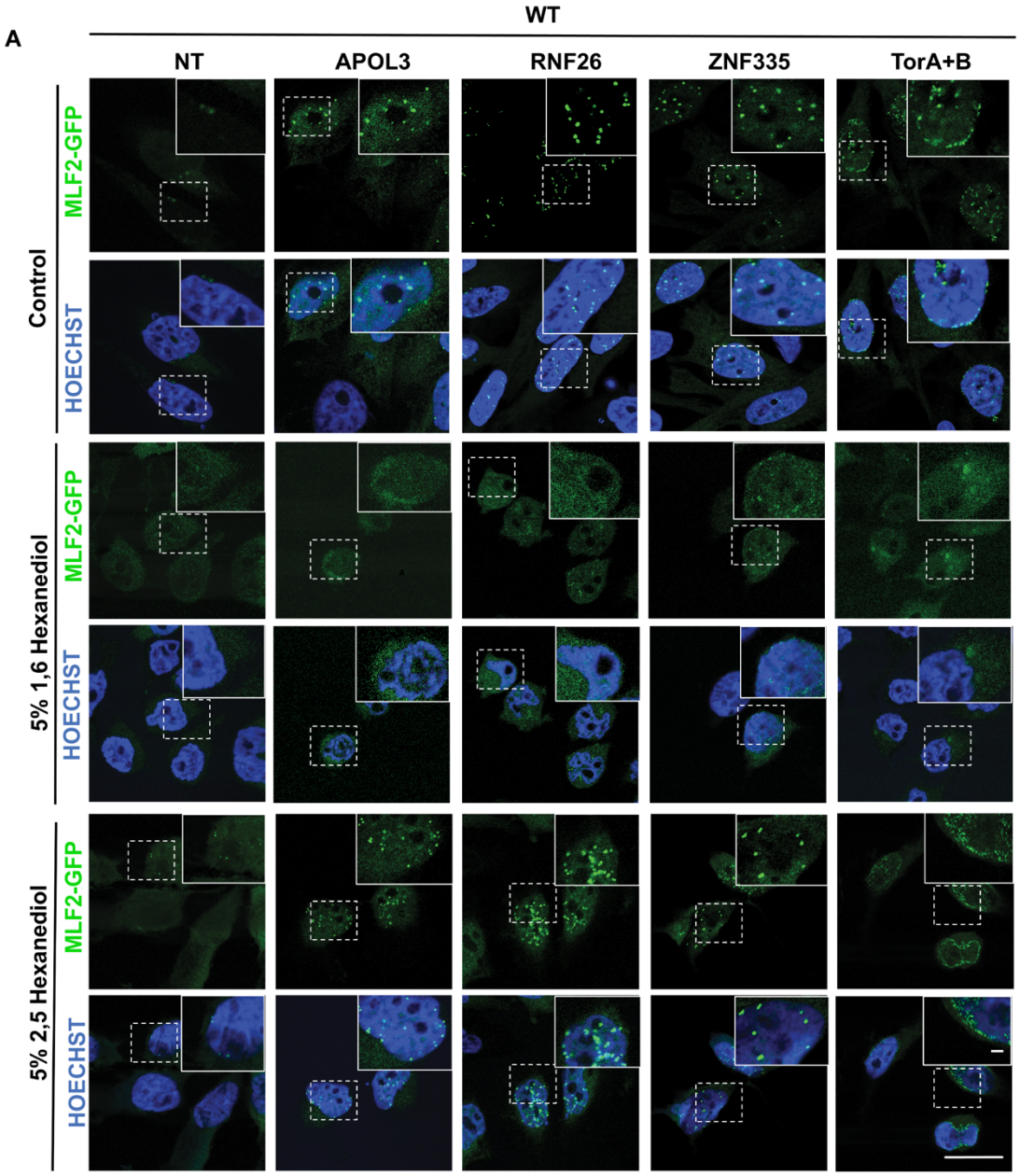
A
WT
NT
APOL3
RNF26
ZNF335
TorA+B
Control
MLF2-GFP
HOECHST
5% 1,6 Hexanediol
MLF2-GFP
HOECHST
5% 2,5 Hexanediol
MLF2-GFP
HOECHST

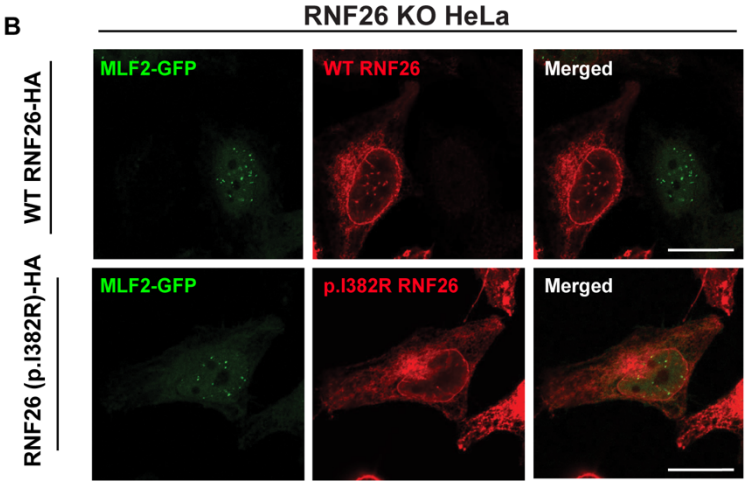
B
RNF26 KO HeLa
WT RNF26-HA
MLF2-GFP
WT RNF26
Merged
RNF26 (p.I382R)-HA
MLF2-GFP
p.I382R RNF26
Merged

Figure S3. Condensates resulting from CRISPR KO can be dissolved by 1,6-Hexanediol and rescued. (A) Fluorescent microscopy images of KO cells were exposed to either an equivalent volume of DMSO (top), 5% 1,6-hexanediol (middle), or 5% 2,5-hexanediol (bottom) for 5 min. WT cells with ZNF335, RNF26, APOL3, and TOR1A/TOR1B knocked out demonstrated dissolution of NE condensates marked by MLF2-GFP (green) after exposure to 5% 1,6-hexanediol (middle) but not DMSO (top) or negative control 5% 2,5-hexanediol (bottom). (B) Only WT RNF26 rescues KO phenotype. Expression of WT RNF26-HA (top) but not inactive RING domain mutant RNF26 I382R-HA (bottom) rescues and decreases condensate formation in RNF26 KO HeLa cells. Condensates were marked by MLF2-GFP (green) and cells immunostained against α-HA (red). Scale bars, 10 µm.

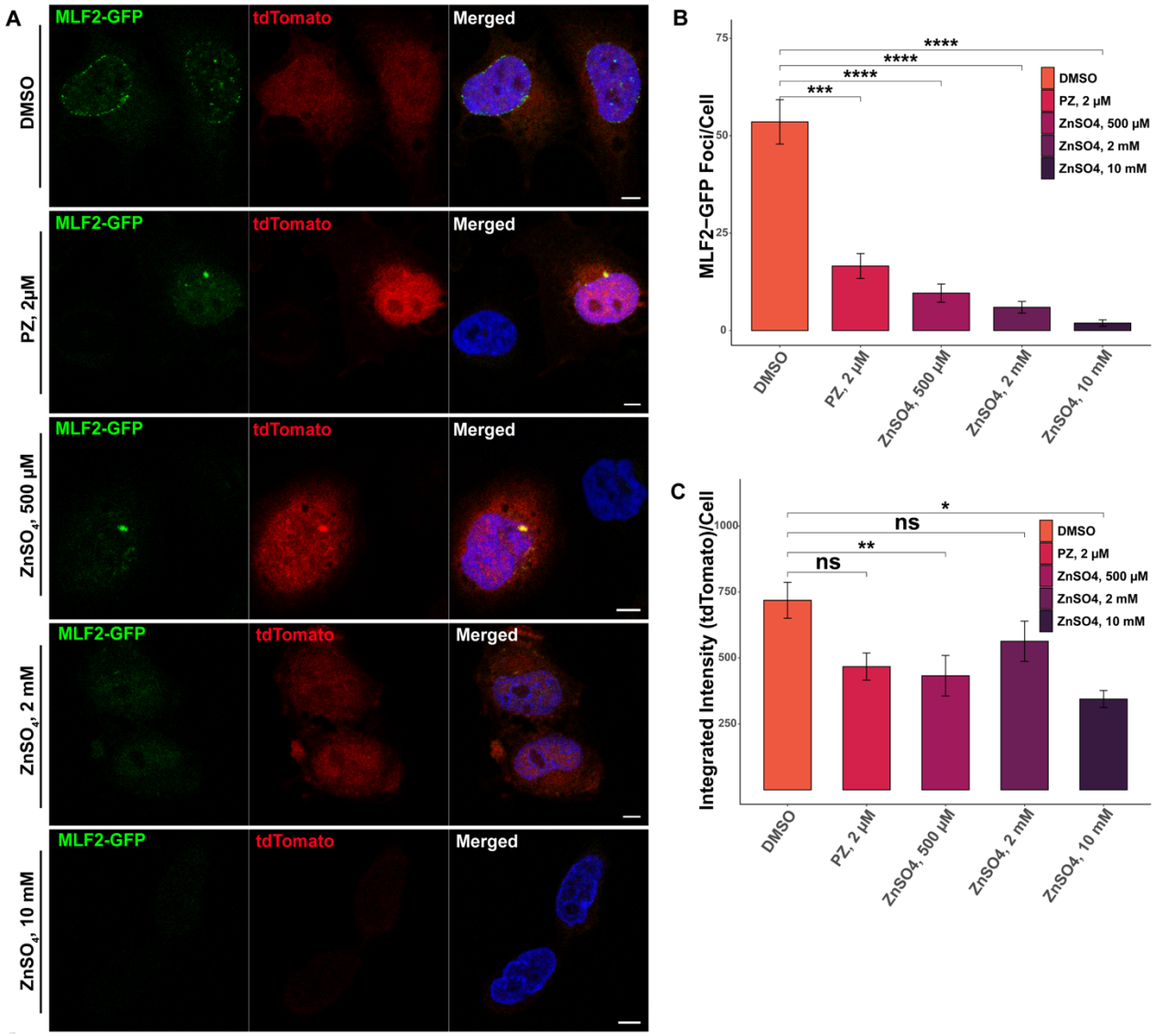

Figure S4. Zinc is sufficient for modulating NE condensates in 4TorKO cells. (A) Figure 6B's associated confocal microscopy images. (B) Quantification of MLF2-GFP foci reduction and (C) of the tdTomato integrated intensity. The fluorescence intensity of the secondary tdTomato reporter (red) and number of MLF2-GFP (green) foci per 4TorKO cell were measured following treatment with 2 µM PZ, 500 µM ZnSO4, 2 mM ZnSO4, or 10 mM ZnSO4 and compared to DMSO-treated controls (3 h). Scale bar, 2 µM. For quantification, black dots represent the number of MLF2-GFP foci per cell (B) or upper quartile integrated tdTomato intensity per cell (C). Asterisks indicate Bonferroni corrected p-values using a Mann-Whitney U test (*: p <= 0.05; **: p <= 0.01; ***: p <= 0.001; ****: p <= 0.0001).

565 **METHODS**
566
567 **Experimental Model and Subject Details**
568
569 **Tissue culture**
570 Adherent cultured cell lines (HeLa and HEK293T) were maintained in Dulbecco's modi-
571 fied Eagle's medium (DMEM) supplemented with 10% (vol/vol) heat-inactivated fetal bo-
572 vine serum (Thermo Fisher Scientific) and 100 units (U) /mL penicillin-streptomycin
573 (Thermo Fisher Scientific). Cells were maintained in either T75 flasks or 10 cm dishes at
574 37℃ (95% humidity; 5% CO_2) and passaged every third day. For splitting, the culture
575 medium was removed, washed once with 1xPBS (Gibco), trypsinized with 0.25% tryp-
576 sin-EDTA (Gibco), and transferred to new dishes (diluted 1:5 or 1:10).
577
578 **Plasmid Constructs**
579 Unless otherwise stated, all plasmid constructs were subcloned into a pcDNA™3.1 (+)
580 Mammalian Expression Vector (Invitrogen, V79020) using standard Gibson Assembly
581 protocols. The cDNA for the MLF2-GFP-P2A-tdTomato construct (MLF2 GenBank ac-
582 cession no. BC000898) was subcloned into the pRetroX-Tight-Pur-GOI (gene of inter-
583 est) vector (Takara Bio) and co-transfected with a pRetroX-Tet-On advanced inducible
584 expression construct (Takara Bio). Viral constructs were co-transfected with both a
585 VSV-G viral envelope plasmid (Addgene #12259) and a psPAX2 viral packaging plas-
586 mid (Addgene #12260). For generation of HeLa cells expressing Cas9-mCherry, an
587 mCherry tag was inserted into the lentiviral plasmid containing Cas9-Flag (Addgene
588 plasmid #52962) immediately after the Flag tag into the BamHI cloning site. Both the se-
589 quences for ZNF335 (KEGG entry hsa: 63925) and RNF26 (KEGG entry hsa: 79102)
590 were subcloned along with a1x-HA tag into a pcDNA3.1(+) vector. Point mutations of
591 ZNF335 (p.Cys467Arg and p.Arg1111His) and RNF26 (p.Ile382Arg) were made using
592 the QuikChange II XL Site-Directed Mutagenesis Kit (#200521, Agilent) following stand-
593 ard QuikChange procedures.
594
595

596 **Lentivirus Production**

597 Lentivirus production was carried out as previously described.[130,131] Briefly, to generate
598 Cas9-flag lentivirus, low-passage HEK293T cells were plated in a 10 cm dish with a
599 density of $3.5x10^6$ cells per dish. Medium was replaced the next day with 6 mL fresh
600 (antibiotic-free) DMEM and transfected with three plasmids encoding: MMLV gag/pol (2
601 µg), viral envelope protein VSV-G (1 µg), and lenti-Cas9-Flag-mCherry (6 µg) using
602 Lipofectamine 2000 (Thermo Fisher Scientific) at a 3:1 ratio of DNA to Lipofectamine.
603 After 72 h, supernatants containing the virus encoding with Cas9-mCherry were har-
604 vested and filtered through a 0.45 µm Steriflip filter unit (MilliporeSigma), aliquoted into
605 screw-cap tubes, and stored at -80°C or used for transduction immediately. For the Dox-
606 inducible MLF2-GFP-P2A-tdTomato system, two separate viruses were produced using
607 three plasmids encoding: MMLV gag/pol (2 µg), viral envelope protein VSV-G (1 µg),
608 and either pRetroX-Tight-MLF2-GFP-P2A-tdTomato or pRetroX-Tet-On (6 µg) using
609 Lipofectamine 3000 (Thermo Fisher Scientific) at a 2:1.5 ratio supplemented with
610 Lipofectamine P3000 (2.5:1). After 72 h, supernatants were collected, stored, or used,
611 as described.

612

613 **Generation of stable HeLa cell lines**

614 The detailed protocol regarding the Tor1A/1B/2A/3A KO and integration of a Dox-induci-
615 ble MLF2-GFP reporter in HeLa cells has been extensively described by our lab
616 (Laudermilch et al. 2016; Rampello et al. 2020).[40,41] The Cas9-flag-mCherry HeLa and
617 Dox-inducible MLF2-GFP-P2A-tdTomato 4TorKO HeLa cell lines were generated by
618 seeding Dox-inducible MLF2-GFP WT HeLa or 4TorKO cells in six-well plates. The next
619 day, media was replaced with DMEM (antibiotic-free) supplemented with 4 µg/mL
620 polybrene (Sigma-Aldrich), and 100 µl of either the Cas9-Flag-mCherry virus (WT HeLa)
621 or both 100 µL of the MLF2-GFP-P2A-tdTomato and pRetro-Tet-On viruses (4TorKO)
622 added dropwise to wells. Medium was replaced 48 hours after transduction (complete
623 DMEM) and grown for another 24 hours. Cells were collected in sorting buffer (ice-cold
624 1xPBS, Gibco) and filtered through a 40 µm nylon mesh filter. Using a BD FACS Aria III,
625 cells were sorted as single cells by selecting those high in either mCherry (WT HeLa) or
626 MLF2-GFP/tdTomato (4TorKO, 16 h after 0.5ug/mL Dox induction) fluorescence

627 intensity. A stringent gating strategy was applied to enrich for cells positive for the re-
628 spective fluorophores while excluding those with extremely high signal intensity, to ob-
629 tain a pure yet physiologically representative population.
630
631 **High-content phenotypic screening strategy**
632 All high-content screening was performed at Yale's Center for Molecular Discovery
633 (YCMD). The Horizon Discovery Edit-R synthetic sgRNA library was used in the whole
634 genome CRISPR KO screen, targeting 19,195 human genes, and comprising of the
635 Drug Targets library (3,683 genes, GA-004650-E2, Lot 20126), the Druggable Genome
636 library (4,643 genes, GA-004670-E2, Lot 20120), and the Human Genome library
637 (10,869 genes, GA-006500-E2, Lot 20130). Each screening plate included 16 replicates
638 of the negative control (NT sgRNA) and 16 replicates of the positive control (combined
639 Tor1A and Tor1B sgRNAs). To ensure robust KO, a pool of three sgRNAs targeting the
640 same gene at different regions was pre-plated into each arrayed well of 384-well glass-
641 bottom plates (Cellvis, #384-1.5H-N). Addition of sgRNA to screening plates was done
642 using the Labcyte Echo 550 Acoustic Dispenser (Labcyte, now Beckman) at a final con-
643 centration of 25 nM.
644 Reverse transfection was performed using DharmaFECT1 Transfection Reagent
645 (Horizon/Dharmacon), which was diluted at 1:500 in Opti-MEM (Thermo Fisher Scien-
646 tific) and mixed with sgRNA. The mixture of sgRNA and transfection reagent was incu-
647 bated for 30 minutes, following which, 2,000 cells/well (WT HeLa integrated with
648 Cas9/MLF2-GFP) in antibiotic-free DMEM were added using a Thermo MultiDrop
649 Combi (Thermo Fisher Scientific). The plates were then incubated for 72 hours at 37°C.
650 To induce MLF2-GFP reporter expression, 0.5 µg/mL Dox was added to each well 16 h
651 before fixation. Media was removed and cells washed once with PBS and fixed with 4%
652 paraformaldehyde (PFA) for 20 minutes. Cells were washed twice with PBS, permea-
653 bilized with 0.1% Triton X-100 for 5 minutes, and washed again with PBS. Cells were
654 stained with Hoechst 33342 dye (1:1000) (Invitrogen, H1399) and HCS CellMask Deep
655 Red Stain (Invitrogen, H32721) (1:5000 of 10 mg/mL, Thermo Fisher Scientific) diluted
656 in PBS for 30 minutes, and washed a final time in PBS. The Molecular Devices ImageX-
657 press 4.0 high-throughput fluorescent microscope (40x magnification) was used to

658 obtain 9-image sets (each consisting of DAPI, MLF2-GFP, and Deep Red CellMask im-
659 ages) per well, resulting in 10,368 TIFF images/plate. Images were uploaded to Yale's
660 McCleary high-performance computing cluster (Yale Center for Research Computing)
661 for analysis.
662 For chemical screening, the Pharmakon 1760 drug library (MicroSource Discov-
663 ery Systems, Inc.) was used, consisting of 1360 FDA-approved drugs and 400 Interna-
664 tional drugs on six 384-well plates. Each screening plate consisted of 16 replicates of
665 the negative control (4TorKO HeLa cells treated with DMSO [0.1% v/v]) and 16 repli-
666 cates of the positive control (WT HeLa cells treated with DMSO [0.1% v/v]). Plates were
667 seeded with 4,000 HeLa cells/well (Multidrop Combi) in 20 µL of DMEM before incubat-
668 ing at 37°C for 24 h. MLF2-GFP expression was induced by adding 0.5 µg/mL of Dox
669 into each well 8 h prior to fixation. Compounds were resuspended in DMSO and added
670 to each well 2 h prior to fixation using a Labcyte Echo 550 Acoustic Dispenser (Labcyte,
671 now Beckman), at a final concentration of 10 µM. Cells were washed, fixed, stained,
672 and imaged using the methods outlined above.
673
674 **Quantification and Statistical Analysis**
675
676 **Image segmentation of phenotypic screen data**
677 We created a custom analysis pipeline to segment condensate foci into single cells us-
678 ing the open-source software *CellProfiler 4.2.6.*[55,56] and downstream statistical analysis
679 using *R Studio* (Version 2023.12.1+402).[132] Individual nuclei were distinguished by
680 shape for objects between 30-100 (+4) pixels using an adaptive (40 pixels) Minimum
681 Cross-Entropy thresholding (0.01-1.0 threshold) in *CellProfiler 4*. The cytoplasm of each
682 nucleus was delineated as a secondary object of each nucleus using a watershed algo-
683 rithm with global Otsu thresholding (three classes, foreground; 0-1.0 threshold, thresh-
684 old correction factor = 0.7).[56,133] Each GFP-channel image was enhanced using a white
685 top-hat transform (speckles; maximum 10 pixels), allowing each condensate foci be-
686 tween 1-15 pixels to be detected using adaptive (50 pixels) Otsu thresholding (three
687 classes, foreground; 0.0175-1.0 threshold, threshold correction factor = 1.2). Groups of

688 condensate foci were then distinguished using local intensity and related to their corre-
689 sponding cytoplasm/nuclei.
690 For parallel analysis, a Bash script was developed allowing the execution of mul-
691 tiple headless CellProfiler instances on a SLURM-managed compute cluster. Specifi-
692 cally, after constructing the analysis pipeline in the CellProfiler GUI, the CreateBatch-
693 Files module is used to generate a batch configuration file that defines image metadata
694 and processing instructions. This batch file is then imported to the cluster environment,
695 and all images are registered within a single CellProfiler project in array format, with im-
696 ages from each plate corresponding to a separate SLURM job. This approach enables
697 autonomous analysis of over 1 million high-content images.TIFF images—amounting to
698 multiple terabytes of data—within a matter of hours. Both the CellProfiler pipeline and
699 Bash scripts are open source and available publicly on the SchliekerLab GitHub page
700 as part of the CondenScreen pipeline (https://github.com/SchliekerLab/Condenscreen-
701 v1.1).
702
703 **Statistical analysis of screen data**
704 We developed a condensate screening using a combined *CellProfiler* and *R* pipeline,
705 *CondenScreen*, to statistically analyze all screen data. The *R*-script features an interac-
706 tive GUI allowing the user to select plate size (6-well to 384-well format), plate layout,
707 and input whether the data was taken from a signal “ON” or a signal “OFF” screen. With
708 limited user input, it then automatically iterates through images from each plate and as-
709 signs groups of image sets into their corresponding wells using string parsing. It quanti-
710 fies the average number of condensate foci/cell, the area of condensate relative to total
711 cell area (optional), and the average number of nuclei/image. To control for variations in
712 transfection efficiencies that could inadvertently impact downstream scoring, the pro-
713 gram has an optional filter to select only the top 25% of cells showing the highest (or
714 lowest) signal using the modest assumption that at least 1 out of 4 cells, on average,
715 will have received the sgRNAs of interest. Additionally, for both screens, the image with
716 the highest score was filtered out, as there were several conditions where one image-
717 set had screening aberrations skewing the condition toward a false positive result. For
718 each plate, aggregate statistics of the respective positive and negative controls are

compared, including signal-to-background (SB), standard deviation (SD) of the controls, and the coefficient of variation (CV) of the controls, among others. To determine separation between positive and negative controls, a Z' assay quality score was calculated: $Z' = 1 - (3(\sigma_{PC} + \sigma_{NC})/|\mu_{PC} - \mu_{NC}|)$,[57] where σ_{PC} and σ_{NC} is the SD and μ_{PC} and μ_{NC} is the condensate mean of the positive and negative controls, respectively.

The percent effect of each condition was quantified by either $E\% = ((\overline{x} - \mu)/\mu) \cdot 100$ (for signal "OFF" selection) or $E\% = ((\mu - \overline{x})/\mu) \cdot 100$ (for signal "ON" selection) where $\overline{x}$ is the average number of condensate foci/cell across the screening population of the plate, and μ, is the average number of condensate foci/cell per tested condition. The significance scoring function is automatically changed depending on selection of a signal "ON" vs a signal "OFF" screen, although this can be adjusted.

For signal "ON" screens, the significance of each condition was calculated using the Z-Score to normalize for intraplate variations: $Z = (E\% - \mu_{E\%})/\ \sigma_{E\%}$, where $\mu_{E\%}$ and $\sigma_{E\%}$ represent the population average percent effect and standard deviation, respectively. Since signal "OFF" screens can often have increased variability, the significance of each well was quantified by calculating the BZ-Score. First, B-Scores were computed by applying Tukey's median polish to each plate to remove row, column, and edge effects. The residuals from the median polish were then scaled by the median absolute deviation (MAD) to produce a robust per-well B-score. Then, the BZ-Score was calculated using the following formula: B$Z = (BScore - \mu_{BScore})/\ \sigma_{BScore}$, where μ_{BScore} and σ_{BScore} are the mean and standard deviation of the B-Scores over the entire plate.

To determine how chemical or genetic perturbations alter cell viability, we derived a function to extrapolate differential cellular health by morphological characterization of the nucleus. Specifically, we added several modules to *CellProfiler* to measure the size, shape, intensity, and texture of each nucleus.[55] This is crucial as several compound concentrations had a non-significant effect in changing the total cell count, but greatly disrupted nuclear morphology based on visual inspection. After testing the effects of multiple parameters, we derived the following empirical formula which best represented the data to estimate nuclear health: $NucHealth = \Delta_{CC} + ((100 + \Delta_{CC})/100) \cdot \sum(\Delta_{Area} + \Delta_{FF})/2$, where Δ_{CC} , Δ_{Area}, and Δ_{FF} are the normalized difference in cell count, nuclear area, and nuclear FormFactor (measurement of nuclear irregularity)

compared to the screening population (or DMSO for dose-response), respectively. Normalization was calculated according to: $\Delta_v = ((V - \mu_V)/\mu_V) \cdot 100$, in which *V* is the variable of interest. The equation was derived with the following assumptions and limitations. (1) Changes to the area and FormFactor should be weighted equally, and (2) cell death should be given a higher impact weight over morphological changes.

CondenScreen provides additional downstream inter-plate and intra-plate visualizations using open-source libraries, including *ggplot2* and *ggplate*. The output includes a ranked list of hits, plots of the screening distributions (raw condensate foci/cell and %effect), a Z/BZ-score plot, and individual plate heatmaps for each 384-well plate. Finally, top hits in both screens were inspected manually to ensure quality control and rule out any additional potential screening aberrations. Notably, manual inspection was rarely a reliable measure of hit robustness. In several cases, hits that were initially overlooked during first-pass screening (false negatives) were later validated and correctly identified by the program. The *CondenScreen* platform is publicly available on the SchliekerLab GitHub page: https://github.com/SchliekerLab/Condenscreen-v1.1.

Solubilization of hit compounds

All putative hit compounds were resuspended up to 100 mM in DMSO. The following compounds were solubilized: pyrithione zinc (PZ) (CAS 13463-41-7), celastrol (CAS 34157-83-0), nerol (CAS 106-25-2), spiramycin (CAS 8025-81-8), choline chloride (CAS 67-48-1), disulfiram (CAS 97-77-8), bronopol (CAS 52-51-7), penfluridol (CAS 26864-56-2), plumbagin (CAS 481-42-5), dyphylline (CAS 479-18-5), econazole nitrate (CAS 24169-02-6), ethacrynic acid (CAS 58-54-8), piroctone olamine (CAS 68890-66-4), dihydrocelastryl (CAS 80-97-7), fenipentol (CAS 583-03-9), triclosan (CAS 3380-34-5), eprodisate disodium (CAS 36589-58-9), L-phenylalanine (CAS 63-91-2), nabumetone (CAS 42924-53-8), edrophonium chloride (CAS 116-38-1), josamycin (CAS 16846-24-5), mevastatin (CAS 73573-88-3), clofibric acid (CAS 882-09-7), docosahexaenoic acid (CAS 6217-54-5).

781 **Dose-dependent validation of small molecules**

782 Based on the change in MLF2-GFP foci, viability, and structural diversity, the 22 top-
783 scoring putative hit compounds were resuspended to 100 mM in DMSO. Using analo-
784 gous methods described in the "High-content screening strategy" section, a 12-point
785 dose response was constructed with concentrations ranging from < 100 nM to 100 μM
786 of each compound, with a final working DMSO concentration of 0.1%. All compounds
787 were tested using four replicates, and 12-positive (WT HeLa) and 12-negative (DMSO)
788 controls were included on each screening plate to ensure assay robustness. MLF2-GFP
789 was induced with 0.5 μg/mL of Dox 8 h before fixation, and compounds were added 3 h
790 prior to fixation. Cells were washed, fixed, stained, and imaged as described above. All
791 dose-response images were analyzed using an analogous *CellProfiler* + *R*-script pipe-
792 line.

793 The effect of each concentration was interpolated (*R*, *drc* & *ggplot*) using a four-
794 parameter log-logistic function for each compound: $f(x) = \min + (\max - \min)/(1 +$
795 $e^{h(\log(x) - \log(IC_{50}))})$, where x is the concentration, min represents the lower asymptote,
796 max represents the higher asymptote, IC_{50} is the concentration at which response is
797 50% of the way between min and max, and h is the hill coefficient.[134,135] The percent
798 toxicity was calculated by fitting the additive inverse of the nuclear health function val-
799 ues to the same model.

800

801 **Pathway enrichment analysis**

802 The Search Tool for Interactions of Chemicals (STITCH) database was used to predict
803 proteins that directly or indirectly interact with the hit compounds at high confidence.[58]
804 STITCH integrates chemical-chemical and chemical-protein interactions through experi-
805 mental databases, pathway databases, and natural language text-mining processing
806 approaches. A minimum interaction confidence score of >0.7 ("high confidence") was
807 applied for a total maximum of 50 primary interactors for the combined set of tested
808 compounds.

809 Gene Ontology (GO) term enrichment analysis was used for all primary predicted
810 interacting proteins from the chemical screen and the top 100 CRISPR gene hits.[59] The
811 gene/chemical hits were separately analyzed in *R* to determine enriched biological

812 process pathways using the enrichGO function (*clusterProfiler*).[60] Enriched pathways
813 were compared against an annotation database (org.Hs.eg.db) with a p-value cutoff of
814 0.05, after controlling for false discovery rate using the Benjamini-Hochberg (BH) proce-
815 dure. The top 30 pathways were then plotted using the *pheatmap* function and addition-
816 ally plotted to an interactive .html graphic using heatmaply.[136] Pathways were grouped
817 by hierarchical clustering using Euclidean distance with complete linkage. To explore
818 the interactive heatmap, please visit the SchliekerLab GitHub page and download the
819 corresponding .html files under the "Interactive Figures" folder.
820
821 **Immunofluorescence and confocal microscopy:**
822 HeLa cells were grown on 13 mm round coverslips and fixed with 4% (v/v) paraformal-
823 dehyde (Thermo Fisher Scientific), washed with 1x PBS (Gibco), permeabilized with
824 0.1% (v/v) Triton X-100 (Sigma-Aldrich) for 5 minutes, and blocked with a PBS mixture
825 containing 2% (w/v) BSA and 2% (w/v) glycine. Primary antibodies were diluted in
826 blocking buffer and added dropwise to coverslips for a one-hour incubation. After wash-
827 ing 3x with blocking buffer, fluorescent secondary antibodies diluted in blocking buffer
828 were added for an additional hour, followed by a 1x PBS wash. Coverslips were then
829 stained using a 1:2000 dilution of Hoechst 33342 (Life Technologies). Cells were then
830 washed 3x with PBS before mounting onto slides (Fluoromount-G, Southern Biotech).
831 Primary antibodies were diluted 1:500: anti-HA produced in rat (11867423001, Roche),
832 anti-K48 produced in rabbit (ZRB2150, Millipore Sigma), and anti-Mab414 produced in
833 mouse. Secondary antibodies were conjugated to Alexa Fluor 568 (Life Technologies).
834 Epifluorescence images were captured using a Zeiss AXIO Observer Z1 inverted
835 fluorescence microscope using a ×63/1.40 oil objective. All confocal images were ac-
836 quired at Yale's Imaging Facility on Science Hill using a Zeiss LSM 880 laser scanning
837 confocal microscope with a C Plan-Apochromat ×63/1.40 oil objective. Images were an-
838 alyzed with *CondenScreen* and compiled for publication using Zeiss v3.4 and Image J
839 (Fiji) software.
840
841
842

843 **Validation of hit compounds**

844 Based on the dose-response results, we focused validation efforts on four compounds:
845 PZ (IC_{50} = 601.6 nM), celastrol (IC_{50} = 124.3 nM), disulfiram (IC_{50} = 10.8 μM), and plum-
846 bagin (IC_{50} = 7.41 μM). To determine the optimal concentrations using a tighter set of
847 concentrations, MLF2-GFP expression was induced in 4TorKO HeLa cells (0.5 μg/mL
848 Dox, 8 h) and treated with either DMSO or one of four different concentrations/com-
849 pounds: 2x below the IC_{50}, IC_{50}, 2x above the IC_{50}, or 8x above the IC_{50}. Compounds
850 were added 3 h before fixation. For each condition, images (n > 50 cells/condition) were
851 captured on a Zeiss AXIO Observer Z1 inverted fluorescence microscope and analyzed
852 using our *CellProfiler* pipeline. *R Studio* was used to cluster MLF2-GFP foci into single
853 cells grouped by treatment condition and construct jittered boxplots. To determine the
854 effect of compounds on K48-ubiquitinated proteins accumulation within condensates,
855 we incubated cells with compounds for 3h (PZ, 3 μM; celastrol, 3 μM; plumbagin, 15
856 μM; and disulfiram, 50 μM), followed by immunofluorescent labeling with α-K48 primary
857 antibody (1:500). Images were captured and analyzed as described above. Statistical
858 comparisons between each condition and the DMSO vehicle control were performed us-
859 ing the Mann–Whitney U test, with Bonferroni correction applied for multiple compari-
860 sons. High-resolution representative images were acquired using confocal microscopy
861 (Zeiss LSM 880).

862 To determine differential protein expression, we constructed a 4TorKO HeLa cell
863 line with a Dox inducible MLF2-GFP-P2A-tdTomato marker, where tdTomato serves as
864 a diffuse secondary reporter for global protein synthesis. Cells were induced with 0.5
865 μg/mL Dox and treated with their respective compound for 6 h before fixation. Imaging
866 was carried out on the Zeiss AXIO and the Zeiss LSM 880 for quantification and high-
867 resolution, respectively. The integrated intensity of both GFP and tdTomato signal was
868 quantified (n > 50) with *CellProfiler* and *R*. To ascertain the relative influence of global
869 protein expression inhibition on the reduced number of MLF2-GFP foci, we derived the
870 following empirical equation to determine the condensate normalization score ($CNS =$
871 $(1 - (\overline{F}_x/\overline{F}_{DMSO})) \cdot (\overline{II}_x/\overline{II}_{DMSO})^2$, where $\overline{F}$ and $\overline{II}$ are the average number of NE con-
872 densate foci and the average integrated intensity of the secondary marker, respectively,
873 for either the tested condition (x) or the DMSO control. The scoring system is designed

874 to prioritize compounds that robustly reduce condensate foci without affecting tdTomato
875 reporter expression. It assigns moderate scores to compounds that significantly deplete
876 foci but also modestly reduce tdTomato intensity, and penalizes those that have little ef-
877 fect on foci or substantially suppress reporter expression. The weighting is particularly
878 sensitive to changes in tdTomato intensity due to the squared exponent, thereby
879 strongly penalizing compounds which impair protein expression.
880
881 **Guide RNA-mediated KO and rescue experiments:**
882 Each gene KO consisted of a pool of 3 distinct, synthetic sgRNAs, each targeting a dif-
883 ferent portion of the same gene (Horizon Discovery). Gene knock-out was conducted
884 using either DharmaFECT or DharmaFECT Duo Transfection Reagent (Horizon discov-
885 ery) using Tor1A KO + Tor1B KO as a positive control and NT sgRNAs as a negative
886 control (Horizon discovery). The sgRNAs were transfected into stably-integrated Cas9
887 expressing HeLa cells and incubated for 72 h with a final sgRNA concentration of 50
888 nM. The cells were treated with 0.5 µg/mL Dox to induce the MLF2-GFP expression 6 h
889 before fixation.
890 The pooled sgRNA sequences used were: ZNF335 sgRNAs (SG-016173, Hori-
891 zon Discovery), GATGATGGTGGCGCCGCCCA, GTGCCAGGGTGATCTGCGGT, AC-
892 CAAATGGACCAGGTGCCA; RNF26 sgRNAs (SG-007060, Horizon Discovery),
893 TATCATGGAGGCAGTGTACC, GCATGACATCCTCTCGAAGA, CAGTGTACCTGG-
894 TAGTGAAT; TOR1A sgRNAs (SG-011023, Horizon Discovery)
895 TATGAACATGGCTTTCTGGT, TATGAAGATGGACCTCGCAC, AGTG-
896 CAATGTGGCCACAAAC; and TOR1B sgRNAs (SG-014203-01, Horizon Discovery),
897 AGTGCAGAGTCGATACAAAC, CAAGAGCCGTCTTAGTTATA, TTGGCGGGCCG-
898 GAAGAAAGA.
899 Rescue experiments of the KO phenotypes were assessed by overexpression of
900 either the WT RNF26-HA or WT ZNF225-HA constructs or the corresponding HA-
901 tagged mutants. The number of MLF2-GFP foci for each condition was quantified by us-
902 ing immunofluorescence microscopy with cells being stained against α-HA. Approxi-
903 mately 200 cells per condition were quantified.
904

905 **Sodium arsenite and 1,6-hexanediol treatment**

906 To determine the co-localization of MLF2 into stress granules, Lipofectamine 2000 was
907 used to co-transfect MLF2 with either G3BP1-GFP (Addgene #135997) + MLF2-HA,
908 TDP-43-tdTomato-HA (Addgene #28205) + MLF2-GFP-Flag (Addgene #230986), 3X
909 FLAG-FUS-WT (Addgene #44985) + MLF2-HA, or pcDNA3.1 empty vector + MLF2-
910 GFP (stained against TIA1/TIAR, Rabbit anti-TIAR Cell Signaling 5137S, 1:50 dilution).
911 The next day (16 h post-transfection), HeLa cells were treated with $NaAsO_2$ (0.5 mM)
912 and incubated for 30 min. Cells were fixed for 20 min with PFA, stained, and imaged as
913 outlined. For hexanediol treatment, cells were incubated in complete DMEM medium
914 containing 5% (v/v) 1,6-hexanediol (CAS 629-11-8) or 5% (v/v) 2,5-hexanediol (CAS
915 2935-44-6) for 5 min before fixation and immunofluorescence staining as described.
916

917 **Electron Microscopy:**

918 Electron microscopy was performed at the Center for Cellular and Molecular Imaging,
919 Yale School of Medicine, using our previously described workflow (Laudermilch et al.,
920 2016).[41] Briefly, cells were fixed for 1 h in 2.5% glutaraldehyde in 0.1 M sodium caco-
921 dylate buffer, pH 7.4. Cells were rinsed and scraped in 1% gelatin and centrifuged in a
922 2% agar solution. Chilled cell blocks were processed with osmium and thiocarbohydra-
923 zide-osmium ligand as described (West et al., 2010), and samples were embedded in
924 Durcupan ACM resin (Electron Microscopy Science). Polymerization was performed by
925 incubating samples at 60°C overnight. These blocks were cut into 60 nm sections with a
926 Leica UltraCut UC7 and stained with 2% uranyl acetate and lead citrate on Formvar/car-
927 bon-coated grids. Samples were visualized with an FEI Tecnai Biotwin TEM at 80 kV,
928 and pictures were taken with Morada CCD and iTEM (Olympus) software.
929

930 **CONTRIBUTIONS**

931 D.P., C.M., E.F.E.K., Y.V.S., and C.S. conceptualized and designed experiments. D.P.,
932 C.M., S.M., E.F.E.K., V.T., and N.D. performed the experiments. D.P., C.M., Y.V.S., and
933 C.S. analyzed and interpreted data. D.P., and V.T., developed the computational analy-
934 sis pipeline. D.P. and C.S. wrote the original manuscript. D.P., C.M., S.M., V.T.,
935 E.F.E.K., N.D., Y.V.S., and C.S. edited the manuscript.

936 **AWKNOWLEDGEMENTS**
937 This work was funded by the DOD PR200788 (C.S.) awarded by the U.S. Department
938 of Defense, Department of the Army, along with support from the Dystonia Medical Re-
939 search Foundation. Additionally, this work was supported by the NIH T32 GM145469
940 (D.P.), the European Molecular Biology Organization (EMBO) ALTF 910-2022
941 (E.F.F.K), and the Dutch Research Council (NWO) 019.222EN.007 (E.F.E.K.) This work
942 utilized ImageXpress Micro 4 high content imager that was purchased with funding from
943 a National Institutes of Health SIG grant 1S10OD032384. We thank Morven Graham
944 and the Center for Cellular and Molecular Imaging (CCMI) Electron Microscopy Facility
945 for the collection of TEM images and Shawn Ferguson for sharing stress granule
946 marker reagents. The funders had no role in study design, data collection and analysis,
947 decision to publish or preparation of the manuscript.
948
949 **DECLARATION OF INTEREST**
950 The authors declare no competing interests.

951 **REFERENCES**

952 1. Prophet, S.M., Rampello, A.J., Niescier, R.F., Gentile, J.E., Mallik, S., Koleske, A.J.,
953 and Schlieker, C. (2022). Atypical nuclear envelope condensates linked to neuro-
954 logical disorders reveal nucleoporin-directed chaperone activities. Nat. Cell Biol.
955 *24*, 1630–1641. https://doi.org/10.1038/s41556-022-01001-y.

956 2. Mackenzie, I.R., Nicholson, A.M., Sarkar, M., Messing, J., Purice, M.D., Pottier, C.,
957 Annu, K., Baker, M., Perkerson, R.B., Kurti, A., et al. (2017). TIA1 Mutations in Am-
958 yotrophic Lateral Sclerosis and Frontotemporal Dementia Promote Phase Separa-
959 tion and Alter Stress Granule Dynamics. Neuron *95*, 808-816.e9.
960 https://doi.org/10.1016/j.neuron.2017.07.025.

961 3. Alberti, S., and Dormann, D. (2019). Liquid-Liquid Phase Separation in Disease.
962 Annu. Rev. Genet. *53*, 171–194. https://doi.org/10.1146/annurev-genet-112618-
963 043527.

964 4. Kedersha, N., Stoecklin, G., Ayodele, M., Yacono, P., Lykke-Andersen, J., Fritzler,
965 M.J., Scheuner, D., Kaufman, R.J., Golan, D.E., and Anderson, P. (2005). Stress
966 granules and processing bodies are dynamically linked sites of mRNP remodeling.
967 J. Cell Biol. *169*, 871–884. https://doi.org/10.1083/jcb.200502088.

968 5. Portz, B., Lee, B.L., and Shorter, J. (2021). FUS and TDP-43 Phases in Health and
969 Disease. Trends Biochem. Sci. *46*, 550–563.
970 https://doi.org/10.1016/j.tibs.2020.12.005.

971 6. Alberti, S., Gladfelter, A., and Mittag, T. (2019). Considerations and Challenges in
972 Studying Liquid-Liquid Phase Separation and Biomolecular Condensates. Cell *176*,
973 419–434. https://doi.org/10.1016/j.cell.2018.12.035.

974 7. Mittag, T., and Pappu, R.V. (2022). A conceptual framework for understanding
975 phase separation and addressing open questions and challenges. Mol. Cell *82*,
976 2201–2214. https://doi.org/10.1016/j.molcel.2022.05.018.

977 8. Lafontaine, D.L.J., Riback, J.A., Bascetin, R., and Brangwynne, C.P. (2021). The nu-
978 cleolus as a multiphase liquid condensate. Nat. Rev. Mol. Cell Biol. *22*, 165–182.
979 https://doi.org/10.1038/s41580-020-0272-6.

980 9. Jain, S., Wheeler, J.R., Walters, R.W., Agrawal, A., Barsic, A., and Parker, R.
981 (2016). ATPase-Modulated Stress Granules Contain a Diverse Proteome and Sub-
982 structure. Cell *164*, 487–498. https://doi.org/10.1016/j.cell.2015.12.038.

983 10. Brangwynne, C.P., Eckmann, C.R., Courson, D.S., Rybarska, A., Hoege, C., Gha-
984 rakhani, J., Jülicher, F., and Hyman, A.A. (2009). Germline P granules are liquid
985 droplets that localize by controlled dissolution/condensation. Science *324*, 1729–
986 1732. https://doi.org/10.1126/science.1172046.

11. Schmidt, H.B., and Görlich, D. (2016). Transport Selectivity of Nuclear Pores, Phase Separation, and Membraneless Organelles. Trends Biochem. Sci. *41*, 46–61. https://doi.org/10.1016/j.tibs.2015.11.001.

12. Li, P., Banjade, S., Cheng, H.-C., Kim, S., Chen, B., Guo, L., Llaguno, M., Hollingsworth, J.V., King, D.S., Banani, S.F., et al. (2012). Phase transitions in the assembly of multivalent signalling proteins. Nature *483*, 336–340. https://doi.org/10.1038/nature10879.

13. Wolozin, B., and Ivanov, P. (2019). Stress granules and neurodegeneration. Nat. Rev. Neurosci. *20*, 649–666. https://doi.org/10.1038/s41583-019-0222-5.

14. Alberti, S., and Hyman, A.A. (2021). Biomolecular condensates at the nexus of cellular stress, protein aggregation disease and ageing. Nat. Rev. Mol. Cell Biol. *22*, 196–213. https://doi.org/10.1038/s41580-020-00326-6.

15. Yan, X., Kuster, D., Mohanty, P., Nijssen, J., Pombo-García, K., Morato, J.G., Rizuan, A., Franzmann, T.M., Sergeeva, A., Ly, A.M., et al. (2025). Intra-condensate demixing of TDP-43 inside stress granules generates pathological aggregates. Cell *0*. https://doi.org/10.1016/j.cell.2025.04.039.

16. Vendruscolo, M., and Fuxreiter, M. (2022). Protein condensation diseases: therapeutic opportunities. Nat. Commun. *13*, 5550. https://doi.org/10.1038/s41467-022-32940-7.

17. Ng, S.C., and Görlich, D. (2022). A simple thermodynamic description of phase separation of Nup98 FG domains. Nat. Commun. *13*, 6172. https://doi.org/10.1038/s41467-022-33697-9.

18. Kozai, T., Fernandez-Martinez, J., van Eeuwen, T., Gallardo, P., Kapinos, L.E., Mazur, A., Zhang, W., Tempkin, J., Panatala, R., Delgado-Izquierdo, M., et al. (2023). Dynamic molecular mechanism of the nuclear pore complex permeability barrier. bioRxiv, 2023.03.31.535055. https://doi.org/10.1101/2023.03.31.535055.

19. Dekker, M., Van der Giessen, E., and Onck, P.R. (2023). Phase separation of intrinsically disordered FG-Nups is driven by highly dynamic FG motifs. Proc. Natl. Acad. Sci. *120*, e2221804120. https://doi.org/10.1073/pnas.2221804120.

20. Cowburn, D., and Rout, M. (2023). Improving the hole picture: towards a consensus on the mechanism of nuclear transport. Biochem. Soc. Trans. *51*, 871–886. https://doi.org/10.1042/BST20220494.

21. Frey, S., Richter, R.P., and Görlich, D. (2006). FG-rich repeats of nuclear pore proteins form a three-dimensional meshwork with hydrogel-like properties. Science *314*, 815–817. https://doi.org/10.1126/science.1132516.

1022 22. Hülsmann, B.B., Labokha, A.A., and Görlich, D. (2012). The Permeability of Recon-
1023 stituted Nuclear Pores Provides Direct Evidence for the Selective Phase Model.
1024 Cell *150*, 738–751. https://doi.org/10.1016/j.cell.2012.07.019.

1025 23. Denning, D.P., Patel, S.S., Uversky, V., Fink, A.L., and Rexach, M. (2003). Disorder
1026 in the nuclear pore complex: The FG repeat regions of nucleoporins are natively
1027 unfolded. Proc. Natl. Acad. Sci. *100*, 2450–2455.
1028 https://doi.org/10.1073/pnas.0437902100.

1029 24. Mallik, S., Poch, D., Burick, S., and Schlieker, C. (2024). Protein folding and quality
1030 control during nuclear transport. Curr. Opin. Cell Biol. *90*, 102407.
1031 https://doi.org/10.1016/j.ceb.2024.102407.

1032 25. Coyne, A.N., and Rothstein, J.D. (2022). Nuclear pore complexes — a doorway to
1033 neural injury in neurodegeneration. Nat. Rev. Neurol. *18*, 348–362.
1034 https://doi.org/10.1038/s41582-022-00653-6.

1035 26. Chou, C.-C., Zhang, Y., Umoh, M.E., Vaughan, S.W., Lorenzini, I., Liu, F., Sayegh,
1036 M., Donlin-Asp, P.G., Chen, Y.H., Duong, D.M., et al. (2018). TDP-43 pathology
1037 disrupts nuclear pore complexes and nucleocytoplasmic transport in ALS/FTD. Nat.
1038 Neurosci. *21*, 228–239. https://doi.org/10.1038/s41593-017-0047-3.

1039 27. Grima, J.C., Daigle, J.G., Arbez, N., Cunningham, K.C., Zhang, K., Ochaba, J.,
1040 Geater, C., Morozko, E., Stocksdale, J., Glatzer, J.C., et al. (2017). Mutant Hun-
1041 tingtin Disrupts the Nuclear Pore Complex. Neuron *94*, 93-107.e6.
1042 https://doi.org/10.1016/j.neuron.2017.03.023.

1043 28. Pappas, S.S., Liang, C.-C., Kim, S., Rivera, C.O., and Dauer, W.T. (2018). TorsinA
1044 dysfunction causes persistent neuronal nuclear pore defects. Hum. Mol. Genet. *27*,
1045 407–420. https://doi.org/10.1093/hmg/ddx405.

1046 29. Zbinden, A., Pérez-Berlanga, M., De Rossi, P., and Polymenidou, M. (2020). Phase
1047 Separation and Neurodegenerative Diseases: A Disturbance in the Force. Dev.
1048 Cell *55*, 45–68. https://doi.org/10.1016/j.devcel.2020.09.014.

1049 30. Kuiper, E.F.E., Prophet, S.M., and Schlieker, C. (2023). Coordinating nucleoporin
1050 condensation and nuclear pore complex assembly. FEBS Lett.
1051 https://doi.org/10.1002/1873-3468.14725.

1052 31. Toyama, B.H., Arrojo e Drigo, R., Lev-Ram, V., Ramachandra, R., Deerinck, T.J.,
1053 Lechene, C., Ellisman, M.H., and Hetzer, M.W. (2018). Visualization of long-lived
1054 proteins reveals age mosaicism within nuclei of postmitotic cells. J. Cell Biol. *218*,
1055 433–444. https://doi.org/10.1083/jcb.201809123.

1056 32. Kim, S., Phan, S., Tran, H.T., Shaw, T.R., Shahmoradian, S.H., Ellisman, M.H., Ve-
1057 atch, S.L., Barmada, S.J., Pappas, S.S., and Dauer, W.T. (2024). TorsinA is essen-
1058 tial for neuronal nuclear pore complex localization and maturation. Nat. Cell Biol.
1059 *26*, 1482–1495. https://doi.org/10.1038/s41556-024-01480-1.

1060 33. Fan, Y., Si, Z., Wang, L., and Zhang, L. (2023). DYT-TOR1A dystonia: an update on
1061 pathogenesis and treatment. Front. Neurosci. *17*, 1216929.
1062 https://doi.org/10.3389/fnins.2023.1216929.

1063 34. Balint, B., Mencacci, N.E., Valente, E.M., Pisani, A., Rothwell, J., Jankovic, J.,
1064 Vidailhet, M., and Bhatia, K.P. (2018). Dystonia. Nat. Rev. Dis. Primer *4*, 1–23.
1065 https://doi.org/10.1038/s41572-018-0023-6.

1066 35. Ozelius, L.J., Hewett, J.W., Page, C.E., Bressman, S.B., Kramer, P.L., Shalish, C.,
1067 de Leon, D., Brin, M.F., Raymond, D., Corey, D.P., et al. (1997). The early-onset
1068 torsion dystonia gene (DYT1) encodes an ATP-binding protein. Nat. Genet. *17*, 40–
1069 48. https://doi.org/10.1038/ng0997-40.

1070 36. Liang, C.-C., Tanabe, L.M., Jou, S., Chi, F., and Dauer, W.T. (2014). TorsinA hypo-
1071 function causes abnormal twisting movements and sensorimotor circuit neuro-
1072 degeneration. J. Clin. Invest. *124*, 3080–3092. https://doi.org/10.1172/JCI72830.

1073 37. Zhao, C., Brown, R.S.H., Chase, A.R., Eisele, M.R., and Schlieker, C. (2013). Regu-
1074 lation of Torsin ATPases by LAP1 and LULL1. Proc. Natl. Acad. Sci. U. S. A. *110*,
1075 E1545–E1554. https://doi.org/10.1073/pnas.1300676110.

1076 38. Brown, R.S.H., Zhao, C., Chase, A.R., Wang, J., and Schlieker, C. (2014). The
1077 mechanism of Torsin ATPase activation. Proc. Natl. Acad. Sci. *111*, E4822–E4831.
1078 https://doi.org/10.1073/pnas.1415271111.

1079 39. Demircioglu, F.E., Sosa, B.A., Ingram, J., Ploegh, H.L., and Schwartz, T.U. (2016).
1080 Structures of TorsinA and its disease-mutant complexed with an activator reveal
1081 the molecular basis for primary dystonia. eLife *5*, e17983.
1082 https://doi.org/10.7554/eLife.17983.

1083 40. Rampello, A.J., Laudermilch, E., Vishnoi, N., Prophet, S.M., Shao, L., Zhao, C.,
1084 Lusk, C.P., and Schlieker, C. (2020). Torsin ATPase deficiency leads to defects in
1085 nuclear pore biogenesis and sequestration of MLF2. J. Cell Biol. *219*, e201910185.
1086 https://doi.org/10.1083/jcb.201910185.

1087 41. Laudermilch, E., Tsai, P.-L., Graham, M., Turner, E., Zhao, C., and Schlieker, C.
1088 (2016). Dissecting Torsin/cofactor function at the nuclear envelope: a genetic
1089 study. Mol. Biol. Cell *27*, 3964–3971. https://doi.org/10.1091/mbc.E16-07-0511.

1090 42. VanGompel, M.J.W., Nguyen, K.C.Q., Hall, D.H., Dauer, W.T., and Rose, L.S.
1091 (2015). A novel function for the Caenorhabditis elegans torsin OOC-5 in nucleo-
1092 porin localization and nuclear import. Mol. Biol. Cell *26*, 1752–1763.
1093 https://doi.org/10.1091/mbc.E14-07-1239.

1094 43. Jokhi, V., Ashley, J., Nunnari, J., Noma, A., Ito, N., Wakabayashi-Ito, N., Moore,
1095 M.J., and Budnik, V. (2013). Torsin Mediates Primary Envelopment of Large Ribo-
1096 nucleoprotein Granules at the Nuclear Envelope. Cell Rep. *3*, 988–995.
1097 https://doi.org/10.1016/j.celrep.2013.03.015.

1098 44. Ding, B., Tang, Y., Ma, S., Akter, M., Liu, M.-L., Zang, T., and Zhang, C.-L. (2021).
1099 Disease Modeling with Human Neurons Reveals LMNB1 Dysregulation Underlying
1100 DYT1 Dystonia. J. Neurosci. *41*, 2024–2038. https://doi.org/10.1523/JNEURO-
1101 SCI.2507-20.2020.

1102 45. Goodchild, R.E., Kim, C.E., and Dauer, W.T. (2005). Loss of the Dystonia-Associ-
1103 ated Protein TorsinA Selectively Disrupts the Neuronal Nuclear Envelope. Neuron
1104 *48*, 923–932. https://doi.org/10.1016/j.neuron.2005.11.010.

1105 46. Kuiper, E.F.E., Gallardo, P., Bergsma, T., Mari, M., Kolbe Musskopf, M., Kuipers, J.,
1106 Giepmans, B.N.G., Steen, A., Kampinga, H.H., Veenhoff, L.M., et al. (2022). The
1107 chaperone DNAJB6 surveils FG-nucleoporins and is required for interphase nu-
1108 clear pore complex biogenesis. Nat. Cell Biol. *24*, 1584–1594.
1109 https://doi.org/10.1038/s41556-022-01010-x.

1110 47. Frey, S., Rees, R., Schünemann, J., Ng, S.C., Fünfgeld, K., Huyton, T., and Görlich,
1111 D. (2018). Surface Properties Determining Passage Rates of Proteins through Nu-
1112 clear Pores. Cell *174*, 202-217.e9. https://doi.org/10.1016/j.cell.2018.05.045.

1113 48. Martin, E.W., Holehouse, A.S., Peran, I., Farag, M., Incicco, J.J., Bremer, A., Grace,
1114 C.R., Soranno, A., Pappu, R.V., and Mittag, T. (2020). Valence and patterning of
1115 aromatic residues determine the phase behavior of prion-like domains. Science
1116 *367*, 694–699. https://doi.org/10.1126/science.aaw8653.

1117 49. Colombrita, C., Zennaro, E., Fallini, C., Weber, M., Sommacal, A., Buratti, E., Silani,
1118 V., and Ratti, A. (2009). TDP-43 is recruited to stress granules in conditions of oxi-
1119 dative insult. J. Neurochem. *111*, 1051–1061. https://doi.org/10.1111/j.1471-
1120 4159.2009.06383.x.

1121 50. Palangi, F., Samuel, S.M., Thompson, I.R., Triggle, C.R., and Emara, M.M. (2017).
1122 Effects of oxidative and thermal stresses on stress granule formation in human in-
1123 duced pluripotent stem cells. PLOS ONE *12*, e0182059.
1124 https://doi.org/10.1371/journal.pone.0182059.

1125 51. Fang, M.Y., Markmiller, S., Vu, A.Q., Javaherian, A., Dowdle, W.E., Jolivet, P.,
1126 Bushway, P.J., Castello, N.A., Baral, A., Chan, M.Y., et al. (2019). Small-Molecule
1127 Modulation of TDP-43 Recruitment to Stress Granules Prevents Persistent TDP-43
1128 Accumulation in ALS/FTD. Neuron *103*, 802-819.e11. https://doi.org/10.1016/j.neu-
1129 ron.2019.05.048.

1130 52. Uechi, H., Sridharan, S., Nijssen, J., Bilstein, J., Iglesias-Artola, J.M., Kishigami, S.,
1131 Casablancas-Antras, V., Poser, I., Martinez, E.J., Boczek, E., et al. (2025). Small-
1132 molecule dissolution of stress granules by redox modulation benefits ALS models.
1133 Nat. Chem. Biol., 1–12. https://doi.org/10.1038/s41589-025-01893-5.

1134 53. Bergsma, T., Steen, A., Kamenz, J.L., Otto, T.A., Gallardo, P., and Veenhoff, L.M.
1135 (2024). Imaging-based quantitative assessment of biomolecular condensates

in vitro and in cells. J. Biol. Chem. *301*, 108130. https://doi.org/10.1016/j.jbc.2024.108130.

54. Baggett, D.W., Medyukhina, A., Tripathi, S., Shirnekhi, H.K., Wu, H., Pounds, S.B., Khairy, K., and Kriwacki, R. (2022). An Image Analysis Pipeline for Quantifying the Features of Fluorescently-Labeled Biomolecular Condensates in Cells. Front. Bioinforma. *2*. https://doi.org/10.3389/fbinf.2022.897238.

55. Stirling, D.R., Swain-Bowden, M.J., Lucas, A.M., Carpenter, A.E., Cimini, B.A., and Goodman, A. (2021). CellProfiler 4: improvements in speed, utility and usability. BMC Bioinformatics *22*, 433. https://doi.org/10.1186/s12859-021-04344-9.

56. Carpenter, A.E., Jones, T.R., Lamprecht, M.R., Clarke, C., Kang, I.H., Friman, O., Guertin, D.A., Chang, J.H., Lindquist, R.A., Moffat, J., et al. (2006). CellProfiler: image analysis software for identifying and quantifying cell phenotypes. Genome Biol. *7*, R100. https://doi.org/10.1186/gb-2006-7-10-r100.

57. Zhang, J.-H., Chung, T.D.Y., and Oldenburg, K.R. (1999). A Simple Statistical Parameter for Use in Evaluation and Validation of High Throughput Screening Assays. J. Biomol. Screen. *4*, 67–73. https://doi.org/10.1177/108705719900400206.

58. Szklarczyk, D., Santos, A., von Mering, C., Jensen, L.J., Bork, P., and Kuhn, M. (2016). STITCH 5: augmenting protein–chemical interaction networks with tissue and affinity data. Nucleic Acids Res. *44*, D380–D384. https://doi.org/10.1093/nar/gkv1277.

59. Ashburner, M., Ball, C.A., Blake, J.A., Botstein, D., Butler, H., Cherry, J.M., Davis, A.P., Dolinski, K., Dwight, S.S., Eppig, J.T., et al. (2000). Gene Ontology: tool for the unification of biology. Nat. Genet. *25*, 25–29. https://doi.org/10.1038/75556.

60. Wu, T., Hu, E., Xu, S., Chen, M., Guo, P., Dai, Z., Feng, T., Zhou, L., Tang, W., Zhan, L., et al. (2021). clusterProfiler 4.0: A universal enrichment tool for interpreting omics data. The Innovation *2*. https://doi.org/10.1016/j.xinn.2021.100141.

61. Prophet, S.M., Naughton, B.S., and Schlieker, C. (2022). p97/UBXD1 Generate Ubiquitylated Proteins That Are Sequestered into Nuclear Envelope Herniations in Torsin-Deficient Cells. Int. J. Mol. Sci. *23*, 4627. https://doi.org/10.3390/ijms23094627.

62. Liu, Z., Chen, O., Wall, J.B.J., Zheng, M., Zhou, Y., Wang, L., Ruth Vaseghi, H., Qian, L., and Liu, J. (2017). Systematic comparison of 2A peptides for cloning multi-genes in a polycistronic vector. Sci. Rep. *7*, 2193. https://doi.org/10.1038/s41598-017-02460-2.

63. Martin, H.L., Adams, M., Higgins, J., Bond, J., Morrison, E.E., Bell, S.M., Warriner, S., Nelson, A., and Tomlinson, D.C. (2014). High-Content, High-Throughput Screening for the Identification of Cytotoxic Compounds Based on Cell Morphology

1173 and Cell Proliferation Markers. PLOS ONE *9*, e88338. https://doi.org/10.1371/jour-
1174 nal.pone.0088338.

1175 64. Patel, D.D., Gripp, K.W., Wadman, E., Mishra, I., and Kandula, V. (2024). Novel bial-
1176 lelic ZNF335 variant causing primary microcephaly: A case report and radiological
1177 review. Am. J. Med. Genet. A. *194*, e63593. https://doi.org/10.1002/ajmg.a.63593.

1178 65. Yang, Y.J., Baltus, A.E., Mathew, R.S., Murphy, E.A., Evrony, G.D., Gonzalez, D.M.,
1179 Wang, E.P., Marshall-Walker, C.A., Barry, B.J., Murn, J., et al. (2012). Microceph-
1180 aly Gene Links Trithorax and REST/NRSF to Control Neural Stem Cell Proliferation
1181 and Differentiation. Cell *151*, 1097–1112. https://doi.org/10.1016/j.cell.2012.10.043.

1182 66. Grillet, M., Gonzalez, B.D., Sicart, A., Pöttler, M., Cascalho, A., Billion, K., Diaz,
1183 S.H., Swerts, J., Naismith, T.V., Gounko, N.V., et al. (2016). Torsins Are Essential
1184 Regulators of Cellular Lipid Metabolism. Dev. Cell *38*, 235–247.
1185 https://doi.org/10.1016/j.devcel.2016.06.017.

1186 67. Rampello, A.J., Prophet, S.M., and Schlieker, C. (2020). The Role of Torsin AAA+
1187 Proteins in Preserving Nuclear Envelope Integrity and Safeguarding Against Dis-
1188 ease. Biomolecules *10*, 468. https://doi.org/10.3390/biom10030468.

1189 68. Lecordier, L., Heo, P., Graversen, J.H., Hennig, D., Skytthe, M.K., Cornet d'Elzius,
1190 A., Pincet, F., Pérez-Morga, D., and Pays, E. (2023). Apolipoproteins L1 and L3
1191 control mitochondrial membrane dynamics. Cell Rep. *42*, 113528.
1192 https://doi.org/10.1016/j.celrep.2023.113528.

1193 69. Gaudet, R.G., Zhu, S., Halder, A., Kim, B.-H., Bradfield, C.J., Huang, S., Xu, D., Ma-
1194 miñska, A., Nguyen, T.N., Lazarou, M., et al. (2021). A human apolipoprotein L with
1195 detergent-like activity kills intracellular pathogens. Science *373*, eabf8113.
1196 https://doi.org/10.1126/science.abf8113.

1197 70. Buchwalter, A.L., Liang, Y., and Hetzer, M.W. (2014). Nup50 is required for cell dif-
1198 ferentiation and exhibits transcription-dependent dynamics. Mol. Biol. Cell *25*,
1199 2472–2484. https://doi.org/10.1091/mbc.e14-04-0865.

1200 71. Megat, S., Mora, N., Sanogo, J., Roman, O., Catanese, A., Alami, N.O., Freischmidt,
1201 A., Mingaj, X., De Calbiac, H., Muratet, F., et al. (2023). Integrative genetic analysis
1202 illuminates ALS heritability and identifies risk genes. Nat. Commun. *14*, 342.
1203 https://doi.org/10.1038/s41467-022-35724-1.

1204 72. Hondele, M., Sachdev, R., Heinrich, S., Wang, J., Vallotton, P., Fontoura, B.M.A.,
1205 and Weis, K. (2019). DEAD-box ATPases are global regulators of phase-separated
1206 organelles. Nature *573*, 144–148. https://doi.org/10.1038/s41586-019-1502-y.

1207 73. Shroff, K., Caffall, Z.F., and Calakos, N. (2021). DYT-TOR1A subcellular proteomics
1208 reveals selective vulnerability of the nuclear proteome to cell stress. Neurobiol. Dis.
1209 *158*, 105464. https://doi.org/10.1016/j.nbd.2021.105464.

1210 74. Cremer, T., Jongsma, M.L.M., Trulsson, F., Vertegaal, A.C.O., Neefjes, J., and Ber-
1211 lin, I. (2021). The ER-embedded UBE2J1/RNF26 ubiquitylation complex exerts
1212 spatiotemporal control over the endolysosomal pathway. Cell Rep. *34*.
1213 https://doi.org/10.1016/j.celrep.2020.108659.

1214 75. Cremer, T., Voortman, L.M., Bos, E., Jongsma, M.L., ter Haar, L.R., Akkermans,
1215 J.J., Talavera Ormeño, C.M., Wijdeven, R.H., de Vries, J., Kim, R.Q., et al. (2023).
1216 RNF26 binds perinuclear vimentin filaments to integrate ER and endolysosomal re-
1217 sponses to proteotoxic stress. EMBO J. *42*, e111252.
1218 https://doi.org/10.15252/embj.2022111252.

1219 76. Li, D., Quan, Z., Ni, J., Li, H., and Qing, H. (2023). The many faces of the zinc finger
1220 protein 335 in brain development and immune system. Biomed. Pharmacother.
1221 *165*, 115257. https://doi.org/10.1016/j.biopha.2023.115257.

1222 77. Stouffs, K., Stergachis, A.B., Vanderhasselt, T., Dica, A., Janssens, S., Vandervore,
1223 L., Gheldof, A., Bodamer, O., Keymolen, K., Seneca, S., et al. (2018). Expanding
1224 the clinical spectrum of biallelic ZNF335 variants. Clin. Genet. *94*, 246–251.
1225 https://doi.org/10.1111/cge.13260.

1226 78. Sato, R., Takanashi, J., Tsuyusaki, Y., Kato, M., Saitsu, H., Matsumoto, N., and
1227 Takahashi, T. (2016). Association Between Invisible Basal Ganglia and ZNF335
1228 Mutations: A Case Report. Pediatrics *138*, e20160897.
1229 https://doi.org/10.1542/peds.2016-0897.

1230 79. Caglayan, A.O., Yaghouti, K., Kockaya, T., Kemer, D., Cankaya, T., Ameziane, N.,
1231 Cogulu, O., Coker, M., and Yalcinkaya, C. (2021). Biallelic ZNF335 mutations
1232 cause basal ganglia abnormality with progressive cerebral/cerebellar atrophy. J.
1233 Neurogenet. *35*, 23–28. https://doi.org/10.1080/01677063.2020.1833006.

1234 80. Nishida, T., Mihara, T., Horiki, T., and Ka, K. (2016). Anaesthesia and orphan dis-
1235 ease: primary autosomal recessive microcephaly-10 caused by a mutation in the
1236 ZNF335 gene. Eur. J. Anaesthesiol. *33*, 543–545.
1237 https://doi.org/10.1097/EJA.0000000000000358.

1238 81. Theusch, E., Ting, F.Y., Qin, Y., Stevens, K., Naidoo, D., King, S.M., Yang, N.V.,
1239 Orr, J., Han, B.Y., Cyster, J.G., et al. (2024). Participant-derived cell line tran-
1240 scriptomic analyses and mouse studies reveal a role for ZNF335 in plasma choles-
1241 terol statin response. Genome Med. *16*, 93. https://doi.org/10.1186/s13073-024-
1242 01366-9.

1243 82. Abramson, J., Adler, J., Dunger, J., Evans, R., Green, T., Pritzel, A., Ronneberger,
1244 O., Willmore, L., Ballard, A.J., Bambrick, J., et al. (2024). Accurate structure predic-
1245 tion of biomolecular interactions with AlphaFold 3. Nature *630*, 493–500.
1246 https://doi.org/10.1038/s41586-024-07487-w.

1247 83. Kroschwald, S., Maharana, S., and Simon, A. (2017). Hexanediol: a chemical probe
1248 to investigate the material properties of membrane-less compartments. In Matters
1249 https://doi.org/10.19185/matters.201702000010.

1250 84. Drozdz, M.M., and Vaux, D.J. (2016). Shared mechanisms in physiological and
1251 pathological nucleoplasmic reticulum formation. Nucleus *8*, 34–45.
1252 https://doi.org/10.1080/19491034.2016.1252893.

1253 85. Drozdz, M.M., Jiang, H., Pytowski, L., Grovenor, C., and Vaux, D.J. (2017). For-
1254 mation of a nucleoplasmic reticulum requires de novo assembly of nascent phos-
1255 pholipids and shows preferential incorporation of nascent lamins. Sci. Rep. *7*,
1256 7454. https://doi.org/10.1038/s41598-017-07614-w.

1257 86. Amberger, J.S., Bocchini, C.A., Schiettecatte, F., Scott, A.F., and Hamosh, A.
1258 (2015). OMIM.org: Online Mendelian Inheritance in Man (OMIM®), an online cata-
1259 log of human genes and genetic disorders. Nucleic Acids Res. *43*, D789–D798.
1260 https://doi.org/10.1093/nar/gku1205.

1261 87. Rubinstein, W.S., Maglott, D.R., Lee, J.M., Kattman, B.L., Malheiro, A.J., Ovetsky,
1262 M., Hem, V., Gorelenkov, V., Song, G., Wallin, C., et al. (2013). The NIH genetic
1263 testing registry: a new, centralized database of genetic tests to enable access to
1264 comprehensive information and improve transparency. Nucleic Acids Res. *41*,
1265 D925–D935. https://doi.org/10.1093/nar/gks1173.

1266 88. Jongsma, M.L.M., Berlin, I., Wijdeven, R.H.M., Janssen, L., Janssen, G.M.C.,
1267 Garstka, M.A., Janssen, H., Mensink, M., van Veelen, P.A., Spaapen, R.M., et al.
1268 (2016). An ER-Associated Pathway Defines Endosomal Architecture for Controlled
1269 Cargo Transport. Cell *166*, 152–166. https://doi.org/10.1016/j.cell.2016.05.078.

1270 89. Wang, W.-M., Liu, Z., Liu, A.-J., Wang, Y.-X., Wang, H.-G., An, D., Heng, B., Xie, L.-
1271 H., Duan, J.-L., and Liu, Y.-Q. (2015). The Zinc Ion Chelating Agent TPEN Attenu-
1272 ates Neuronal Death/apoptosis Caused by Hypoxia/ischemia Via Mediating the
1273 Pathophysiological Cascade Including Excitotoxicity, Oxidative Stress, and Inflam-
1274 mation. CNS Neurosci. Ther. *21*, 708–717. https://doi.org/10.1111/cns.12428.

1275 90. Mann, J.J., and Fraker, P.J. (2005). Zinc pyrithione induces apoptosis and increases
1276 expression of Bim. Apoptosis *10*, 369–379. https://doi.org/10.1007/s10495-005-
1277 0811-9.

1278 91. Lamore, S.D., and Wondrak, G.T. (2011). Zinc pyrithione impairs zinc homeostasis
1279 and upregulates stress response gene expression in reconstructed human epider-
1280 mis. Biometals Int. J. Role Met. Ions Biol. Biochem. Med. *24*, 875–890.
1281 https://doi.org/10.1007/s10534-011-9441-6.

1282 92. Mathieu, C., Pappu, R.V., and Taylor, J.P. (2020). Beyond aggregation: Pathological
1283 phase transitions in neurodegenerative disease. Science *370*, 56–60.
1284 https://doi.org/10.1126/science.abb8032.

1285 93. Thomsen, M., Ott, F., Loens, S., Kilic-Berkmen, G., Tan, A.H., Lim, S.-Y., Lohmann,
1286 E., Schröder, K.M., Ipsen, L., Nothacker, L.A., et al. (2024). Genetic Diversity and
1287 Expanded Phenotypes in Dystonia: Insights from Large-Scale Exome Sequencing.
1288 medRxiv, 2024.12.02.24316741. https://doi.org/10.1101/2024.12.02.24316741.

1289 94. Zech, M., Dzinovic, I., Skorvanek, M., Harrer, P., Necpal, J., Kopajtich, R., Kittke, V.,
1290 Tilch, E., Zhao, C., Tsoma, E., et al. (2025). Combined genomics and proteomics
1291 unveils elusive variants and vast aetiologic heterogeneity in dystonia. Brain,
1292 awaf059. https://doi.org/10.1093/brain/awaf059.

1293 95. Mitrea, D.M., Mittasch, M., Gomes, B.F., Klein, I.A., and Murcko, M.A. (2022). Modu-
1294 lating biomolecular condensates: a novel approach to drug discovery. Nat. Rev.
1295 Drug Discov. *21*, 841–862. https://doi.org/10.1038/s41573-022-00505-4.

1296 96. Patel, A., Mitrea, D., Namasivayam, V., Murcko, M.A., Wagner, M., and Klein, I.A.
1297 (2022). Principles and functions of condensate modifying drugs. Front. Mol. Biosci.
1298 *9*. https://doi.org/10.3389/fmolb.2022.1007744.

1299 97. Rayman, J.B., Karl, K.A., and Kandel, E.R. (2018). TIA-1 Self-Multimerization,
1300 Phase Separation, and Recruitment into Stress Granules Are Dynamically Regu-
1301 lated by Zn2+. Cell Rep. *22*, 59–71. https://doi.org/10.1016/j.celrep.2017.12.036.

1302 98. Singh, V., Xu, L., Boyko, S., Surewicz, K., and Surewicz, W.K. (2020). Zinc pro-
1303 motes liquid–liquid phase separation of tau protein. J. Biol. Chem. *295*, 5850–5856.
1304 https://doi.org/10.1074/jbc.AC120.013166.

1305 99. Kim, K.-R., Park, S.E., Hong, J.-Y., Koh, J.-Y., Cho, D.-H., Hwang, J.J., and Kim, Y.-
1306 H. (2022). Zinc enhances autophagic flux and lysosomal function through transcrip-
1307 tion factor EB activation and V-ATPase assembly. Front. Cell. Neurosci. *16*,
1308 895750. https://doi.org/10.3389/fncel.2022.895750.

1309 100. Liu, X., Zhao, P., Wang, X., Wang, L., Zhu, Y., Song, Y., and Gao, W. (2019).
1310 Celastrol mediates autophagy and apoptosis via the ROS/JNK and Akt/mTOR sig-
1311 naling pathways in glioma cells. J. Exp. Clin. Cancer Res. *38*, 184.
1312 https://doi.org/10.1186/s13046-019-1173-4.

1313 101. Hu, Y., Qian, Y., Wei, J., Jin, T., Kong, X., Cao, H., and Ding, K. (2021). The Disul-
1314 firam/Copper Complex Induces Autophagic Cell Death in Colorectal Cancer by Tar-
1315 geting ULK1. Front. Pharmacol. *12*, 752825.
1316 https://doi.org/10.3389/fphar.2021.752825.

1317 102. Li, Y.-C., He, S.-M., He, Z.-X., Li, M., Yang, Y., Pang, J.-X., Zhang, X., Chow, K.,
1318 Zhou, Q., Duan, W., et al. (2014). Plumbagin induces apoptotic and autophagic cell
1319 death through inhibition of the PI3K/Akt/mTOR pathway in human non-small cell
1320 lung cancer cells. Cancer Lett. *344*, 239–259. https://doi.org/10.1016/j.can-
1321 let.2013.11.001.

1322 103. Xu, K.-H., and Lu, D.-P. (2010). Plumbagin induces ROS-mediated apoptosis in hu-
1323 man promyelocytic leukemia cells in vivo. Leuk. Res. *34*, 658–665.
1324 https://doi.org/10.1016/j.leukres.2009.08.017.

1325 104. Cen, D., Gonzalez, R.I., Buckmeier, J.A., Kahlon, R.S., Tohidian, N.B., and
1326 Meyskens, F.L. (2002). Disulfiram induces apoptosis in human melanoma cells: a
1327 redox-related process. Mol. Cancer Ther. *1*, 197–204.

1328 105. Bernier, M., Harney, D., Koay, Y.C., Diaz, A., Singh, A., Wahl, D., Pulpitel, T., Ali,
1329 A., Guiterrez, V., Mitchell, S.J., et al. (2020). Elucidating the mechanisms by which
1330 disulfiram protects against obesity and metabolic syndrome. Npj Aging Mech. Dis.
1331 *6*, 1–11. https://doi.org/10.1038/s41514-020-0046-6.

1332 106. Cascão, R., Fonseca, J.E., and Moita, L.F. (2017). Celastrol: A Spectrum of Treat-
1333 ment Opportunities in Chronic Diseases. Front. Med. *4*.
1334 https://doi.org/10.3389/fmed.2017.00069.

1335 107. Petrocelli, G., Marrazzo, P., Bonsi, L., Facchin, F., Alviano, F., and Canaider, S.
1336 (2023). Plumbagin, a Natural Compound with Several Biological Effects and Anti-
1337 Inflammatory Properties. Life *13*, 1303. https://doi.org/10.3390/life13061303.

1338 108. Westerheide, S.D., Bosman, J.D., Mbadugha, B.N.A., Kawahara, T.L.A., Matsu-
1339 moto, G., Kim, S., Gu, W., Devlin, J.P., Silverman, R.B., and Morimoto, R.I. (2004).
1340 Celastrols as Inducers of the Heat Shock Response and Cytoprotection. J. Biol.
1341 Chem. *279*, 56053–56060. https://doi.org/10.1074/jbc.M409267200.

1342 109. Wang, C., Shi, C., Yang, X., Yang, M., Sun, H., and Wang, C. (2014). Celastrol
1343 suppresses obesity process via increasing antioxidant capacity and improving lipid
1344 metabolism. Eur. J. Pharmacol. *744*, 52–58.
1345 https://doi.org/10.1016/j.ejphar.2014.09.043.

1346 110. Calakos, N., and Caffall, Z.F. (2024). The integrated stress response pathway and
1347 neuromodulator signaling in the brain: lessons learned from dystonia. J. Clin. In-
1348 vest. *134*. https://doi.org/10.1172/JCI177833.

1349 111. Calakos, N., and Zech, M. (2025). Emerging Molecular-Genetic Families in Dysto-
1350 nia: Endosome-Autophagosome-Lysosome and Integrated Stress Response Path-
1351 ways. Mov. Disord. *40*, 7–21. https://doi.org/10.1002/mds.30037.

1352 112. Gonzalez-Latapi, P., Marotta, N., and Mencacci, N.E. (2021). Emerging and con-
1353 verging molecular mechanisms in dystonia. J. Neural Transm. *128*, 483–498.
1354 https://doi.org/10.1007/s00702-020-02290-z.

1355 113. Martin, J.N., Bair, T.B., Bode, N., Dauer, W.T., and Gonzalez-Alegre, P. (2009).
1356 Transcriptional and proteomic profiling in a cellular model of DYT1 dystonia. Neuro-
1357 science *164*, 563–572. https://doi.org/10.1016/j.neuroscience.2009.07.068.

114. Bjørkøy, G., Lamark, T., Brech, A., Outzen, H., Perander, M., Overvatn, A., Stenmark, H., and Johansen, T. (2005). p62/SQSTM1 forms protein aggregates degraded by autophagy and has a protective effect on huntingtin-induced cell death. J. Cell Biol. *171*, 603–614. https://doi.org/10.1083/jcb.200507002.

115. Wang, Z., and Zhang, H. (2019). Phase Separation, Transition, and Autophagic Degradation of Proteins in Development and Pathogenesis. Trends Cell Biol. *29*, 417–427. https://doi.org/10.1016/j.tcb.2019.01.008.

116. Caffall, Z.F., Wilkes, B.J., Hernández-Martinez, R., Rittiner, J.E., Fox, J.T., Wan, K.K., Shipman, M.K., Titus, S.A., Zhang, Y.-Q., Patnaik, S., et al. (2021). The HIV protease inhibitor, ritonavir, corrects diverse brain phenotypes across development in mouse model of DYT-TOR1A dystonia. Sci. Transl. Med. *13*, eabd3904. https://doi.org/10.1126/scitranslmed.abd3904.

117. Rose, A., and Schlieker, C. (2012). Alternative nuclear transport for cellular protein quality control. Trends Cell Biol. *22*, 509–514. https://doi.org/10.1016/j.tcb.2012.07.003.

118. Mannino, P.J., and Lusk, C.P. (2022). Quality control mechanisms that protect nuclear envelope identity and function. J. Cell Biol. *221*, e202205123. https://doi.org/10.1083/jcb.202205123.

119. Tomioka, Y., Kotani, T., Kirisako, H., Oikawa, Y., Kimura, Y., Hirano, H., Ohsumi, Y., and Nakatogawa, H. (2020). TORC1 inactivation stimulates autophagy of nucleoporin and nuclear pore complexes. J. Cell Biol. *219*, e201910063. https://doi.org/10.1083/jcb.201910063.

120. Lee, C.-W., Wilfling, F., Ronchi, P., Allegretti, M., Mosalaganti, S., Jentsch, S., Beck, M., and Pfander, B. (2020). Selective autophagy degrades nuclear pore complexes. Nat. Cell Biol. *22*, 159–166. https://doi.org/10.1038/s41556-019-0459-2.

121. Martin, C.-A., Murray, J.E., Carroll, P., Leitch, A., Mackenzie, K.J., Halachev, M., Fetit, A.E., Keith, C., Bicknell, L.S., Fluteau, A., et al. (2016). Mutations in genes encoding condensin complex proteins cause microcephaly through decatenation failure at mitosis. Genes Dev. *30*, 2158–2172. https://doi.org/10.1101/gad.286351.116.

122. Shaheen, R., Maddirevula, S., Ewida, N., Alsahli, S., Abdel-Salam, G.M.H., Zaki, M.S., Tala, S.A., Alhashem, A., Softah, A., Al-Owain, M., et al. (2019). Genomic and phenotypic delineation of congenital microcephaly. Genet. Med. *21*, 545–552. https://doi.org/10.1038/s41436-018-0140-3.

123. Pavinato, L., Carestiato, S., Trajkova, S., Sorasio, L., Mantovani, G., De Sanctis, L., Kerkhof, J., McConkey, H., Rzasa, J., Todd, E., et al. (2025). Skipping of Exon 20 in EP300: A Novel Variant Linked to Rubinstein–Taybi Syndrome With Atypical

and Severe Clinical Manifestations. Clin. Genet. *107*, 354–358. https://doi.org/10.1111/cge.14654.

124. Roessler, E., Belloni, E., Gaudenz, K., Jay, P., Berta, P., Scherer, S.W., Tsui, L.C., and Muenke, M. (1996). Mutations in the human Sonic Hedgehog gene cause holoprosencephaly. Nat. Genet. *14*, 357–360. https://doi.org/10.1038/ng1196-357.

125. Loo, C.K.C., Pearen, M.A., and Ramm, G.A. (2021). The Role of Sonic Hedgehog in Human Holoprosencephaly and Short-Rib Polydactyly Syndromes. Int. J. Mol. Sci. *22*, 9854. https://doi.org/10.3390/ijms22189854.

126. Demmerle, J., Hao ,Siyuan, and Cai, D. (2023). Transcriptional condensates and phase separation: condensing information across scales and mechanisms. Nucleus *14*, 2213551. https://doi.org/10.1080/19491034.2023.2213551.

127. Hnisz, D., Shrinivas, K., Young, R.A., Chakraborty, A.K., and Sharp, P.A. (2017). A phase separation model predicts key features of transcriptional control. Cell *169*, 13–23. https://doi.org/10.1016/j.cell.2017.02.007.

128. Fouix, S., Martin-Lannerée, S., Sanial, M., Morla, L., Lamour-Isnard, C., and Plessis, A. (2003). Over-expression of a novel nuclear interactor of Suppressor of fused, the Drosophila myelodysplasia/myeloid leukaemia factor, induces abnormal morphogenesis associated with increased apoptosis and DNA synthesis. Genes Cells Devoted Mol. Cell. Mech. *8*, 897–911. https://doi.org/10.1046/j.1365-2443.2003.00685.x.

129. Dyer, J.O., Dutta, A., Gogol, M., Weake, V.M., Dialynas, G., Wu, X., Seidel, C., Zhang, Y., Florens, L., Washburn, M.P., et al. (2017). Myeloid Leukemia Factor acts in a chaperone complex to regulate transcription factor stability and gene expression. J. Mol. Biol. *429*, 2093–2107. https://doi.org/10.1016/j.jmb.2016.10.026.

130. Tsai, P.-L., Cameron, C.J.F., Forni, M.F., Wasko, R.R., Naughton, B.S., Horsley, V., Gerstein, M.B., and Schlieker, C. (2022). Dynamic quality control machinery that operates across compartmental borders mediates the degradation of mammalian nuclear membrane proteins. Cell Rep. *41*, 111675. https://doi.org/10.1016/j.celrep.2022.111675.

131. Tsai, P.-L., Zhao, C., and Schlieker, C. (2019). Methodologies to monitor protein turnover at the inner nuclear membrane. Methods Enzymol. *619*, 47–69. https://doi.org/10.1016/bs.mie.2018.12.033.

132. Ihaka, R., and Gentleman, R. (1996). R: A Language for Data Analysis and Graphics. J. Comput. Graph. Stat. *5*, 299–314. https://doi.org/10.1080/10618600.1996.10474713.

133. Vincent, L., and Soille, P. (1991). Watersheds in digital spaces: an efficient algorithm based on immersion simulations. IEEE Trans. Pattern Anal. Mach. Intell. *13*, 583–598. https://doi.org/10.1109/34.87344.

134. Ritz, C., Baty, F., Streibig, J.C., and Gerhard, D. (2015). Dose-Response Analysis Using R. PLOS ONE *10*, e0146021. https://doi.org/10.1371/journal.pone.0146021.

135. Wickham, H. (2011). ggplot2. WIREs Comput. Stat. *3*, 180–185. https://doi.org/10.1002/wics.147.

136. Galili, T., O'Callaghan, A., Sidi, J., and Sievert, C. (2018). heatmaply: an R package for creating interactive cluster heatmaps for online publishing. Bioinformatics *34*, 1600–1602. https://doi.org/10.1093/bioinformatics/btx657.